



Applying Two Dimensional Spectroscopy to Study the Dynamics of Photo-Excited States in π -Conjugated Polymers

A Thesis submitted for the Honour School of Chemistry: Part II 2019

John L. A. Gardner

Jesus College
University of Oxford

Physical and Theoretical Chemistry Laboratory

Dedication

I dedicate this thesis to my father, who has always inspired me,[¶] and who has taught me to love Chemistry.

Summary

The electronic properties of π -conjugated polymers have led, in recent years, to their incorporation into technologies such as photovoltaic cells, light emitting devices, and even cancer therapy. Of particular relevance and interest is the family of polymers related to poly(*p*-phenylene vinylene), the polymer modelled in this work.

Both experimental and theoretical work has shown that excited electrons produced upon photo-excitation of π -conjugated polymers undergo rapid relaxation within the first picosecond of dynamics. It is important to understand these ultrafast processes in order that the longer-timescale migration dynamics can be fully understood, since it is these migrations which are key to most π -conjugated polymer applications.

Theoretical work published in 2018 has analysed the dynamics occurring during the first 100 fs after excitation. Both exciton-site decoherence and exciton-polaron formation happen within half a $C-C$ vibrational period (10 fs). These are driven by the coupling of the exciton to vibrational modes of the polymer chain, and are thus broadly independent of the external dissipation. Exciton localisation happens over a longer timescale of ~ 100 fs, and is driven solely by external dissipation.

In this work, we investigate numerically whether experimentally obtainable two dimensional electronic coherence spectra can identify and explore these three quantum processes. We have used a disordered Frenkel-Holstein Hamiltonian to model the centre-of-mass wavefunction of the exciton, which gives rise to Anderson-localised eigenstates. We have assumed that the the exciton dynamics are governed by a Lindblad master equation, where the system-bath interaction is mediated via the system vibrational lowering opera-

tors. Numerically, we have used the Time-Evolving Block Decimation (TEBD) method combined with a quantum jump trajectory technique to simulate the evolution described by this equation.

By controlling the system-environment interactions in the quantum model, and by reference to the results for an isolated monomer, we find that those dynamics which are dictated by the Frenkel-Holstein parameters are not visible in 2D spectra. This leads to a new interpretation of these phenomena (exciton-site decoherence and exciton-polaron formation) as partial destructive interference, rather than absolute decay, of eigenstate coherences.

We find that the dynamics dictated by external dissipation, those of vibrational relaxation and of exciton density localisation, are visible in the peaks corresponding to the states initially excited into, but that the incoherent nature of the decay means that the destination of excited states is not obtainable using the technique of two dimensional electronic coherence spectroscopy (2D ECS).

Contents

Summary	i
Acknowledgements	iii
Glossary of Abbreviations	3
1 Introduction	4
2 Modelling of Polymers and Excitons	6
2.1 Theoretical Models	6
2.2 The Frenkel-Holstein Model	7
2.2.1 Frenkel Model	7
2.2.2 Holstein Model	10
2.3 Open Quantum System	11
3 Ultrafast Quantum Dynamics	14
3.1 Phonon Energy Transfer	14
3.2 Exciton-Polaron Formation	14
3.3 Exciton Decoherence	15
3.4 Exciton Localisation	17
4 Theory of Spectroscopy	18
4.1 Linear Absorption Spectroscopy	18
4.2 Two-Dimensional Electronic Coherence Spectroscopy	19
4.2.1 Wave-Packet Analysis	21
4.2.2 Experimental Setup	24
4.2.3 The Spectrum	25
4.3 Double-sided Feynman Diagrams	25
5 Computational Methods	27
5.1 System Representation and Evolution	27
5.1.1 TEBD	27
5.1.2 Trotter Decomposition	29
5.1.3 Quantum Jumps	29
5.2 System-Light Interactions	30
5.3 Efficient Time Signal Calculation	31

5.3.1	Isolated Case	31
5.3.2	Open System Case	34
6	The Discrete Fourier Transform and Signal Processing	37
6.1	The Discrete Fourier Transform	37
6.1.1	Undersampling	38
6.1.2	Peak Separation	38
6.1.3	Spectral Leakage	39
6.2	Signal Processing	40
6.2.1	Spectrum Representation	41
7	Results and Discussion	42
7.1	Isolated Systems	42
7.1.1	Single Monomer	42
7.1.2	Polymers	46
7.2	Open Systems	48
7.2.1	Single Monomer Case	48
7.2.2	Polymers	50
7.3	Discussion	53
8	Conclusions	56

Glossary of Abbreviations

PPV poly(*p*-phenylene vinylene)

LEGS local exciton ground state

QEES quasi extended exciton state

TDSE time dependent Schrödinger equation

SHO simple harmonic oscillator

ZPE zero point energy

GS ground state

GSM ground state manifold

ESM excited state manifold

2D ECS two dimensional electronic coherence spectroscopy

DFT discrete Fourier transform

TEBD time-evolving block decimation

MPS matrix product state

TNT tensor network theory

Chapter 1

Introduction

The first polymer based light emitting diode was manufactured in 1989,² in the modern day, the interaction between conjugated polymers and light can now be found at the heart of many technologies,³⁻⁵ ranging from organic solar cells⁶ to tumour therapies.⁷ Given this rapid incorporation into technological applications, it is predicted that polymers will continue to become more dominant over their inorganic and molecular counterparts, due to their increased affordability, flexibility, tunability and stability whilst providing the same types of optical and electronic properties.⁸

Of primary importance to these properties is a conjugated polymer's ability to absorb light, and transport this energy both along and between chains.⁹ The excited states of conjugated polymers are well described as excitons,¹⁰ the quasi-particle of an electron electrostatically bound to an electron-hole. Thus, in order to fully utilise the predicted potential of polymer devices, the dynamics of these excitons need to be well understood.

Theoretical work¹¹ published in 2018 has investigated the ultrafast quantum dynamics of the excitonic states produced by photoexcitation of the π -conjugated polymer PPV (poly(*p*-phenylene vinylene)). Three distinct processes have been observed:

- **exciton-polaron formation:** assuming Franck-Condon behaviour,¹⁰ the nuclei remain stationary upon excitation, meaning that, at the instant of excitation, no correlation exists between the exciton's centre of mass and the nuclear displacements of the chain. Within the first 10 fs however, exciton-phonon coupling induces a strong correlation between the two, with an exponential fall off in nuclear displacement as

a function of distance away from the exciton's centre of mass.

- **exciton-site decoherence:** at the instant of excitation, the exciton can display long range quantum-coherences over the range of many monomers. Exciton-polaron formation causes these coherences to decay within the first 10 fs of dynamics.
- **exciton density localisation:** over the longer timescale of 100 fs, exciton density is observed to localise. High energy excited states with initial density spanning much of the complete chain are seen to localise dramatically. Low energy excited states already restricted to a small region of the total chain are seen to localise further, as driven by vibrational relaxation.

In their investigation of these processes *Mannouch et al*^[4] have predominantly analysed correlation functions which do not correspond to physically observable entities. The aim of this work is therefore to investigate whether these processes can be seen experimentally. More specifically, can two dimensional electronic coherence spectroscopy be used to probe the relaxation, decoherence and localisation of photo-excited states in PPV?

This thesis is organised as follows: we start by detailing the theory supporting our modelling of the excited states of PPV in Chapter 2 before describing in more detail the aforementioned dynamics that emerge from this model in Chapter 3. We then present a wavepacket analysis formulation of the theory of multi-dimensional spectroscopy in Chapter 4. It is challenging to accurately simulate the quantum dynamics of large systems; we therefore detail the computational procedures we have used in this work to overcome the problem of an exponentially growing Hilbert space in Chapter 5. Also detailed here is the algorithm I have developed to efficiently produce a multi-dimensional time-signal from which the spectrum can be calculated using the discrete Fourier transform, discussed in Chapter 6.

Finally, we present the results of this work in Chapter 7. We find that population loss from both electronically and vibrationally excited states is visible in the broadening of relevant peaks. The incoherent nature of these relaxations means, however, that we can not identify the destination of the excited states as they relax. We have not detected either exciton-polaron formation, or exciton-site decoherence in our simulations.

Chapter 2

Modelling of Polymers and Excitons

Polymer chains are composed of a large number of monomers, which are themselves composed of many atoms. Thus, it is challenging to construct a representation of the polymer that allows for accurate simulation of the excited state dynamics while remaining numerically tractable.

This chapter provides an overview of the model used in this and previous⁹ work to describe the excited states of conjugated polymers and their interactions with the surrounding environment.

2.1 Theoretical Models

In quantum mechanics, the time dependent Schrödinger equation (TDSE),

$$i\hbar \frac{d}{dt}|\psi(t)\rangle = \hat{H}|\psi(t)\rangle, \quad (2.1)$$

describes the time evolution of the wavefunction $|\psi(t)\rangle$. For the majority of systems, and therefore Hamiltonians, an analytical solution to this equation does not exist, but numerically accurate solutions can be found for any system. In practice, however, as the system size increases, the size of the Hilbert space increases exponentially, meaning that finding these solutions becomes computationally intractable. Specifically, for a system composed of L sites, each with with a basis of n states, the total size of the Hilbert space is n^L . However, many systems can be decomposed into two or more separate sub-systems, dramatically reducing the effective size of the Hilbert space. Unfortunately this is **not** the

case for polymers chains, where off-diagonal terms strongly couple neighbouring sites.

This exponentially growing Hilbert space means both that we need to employ efficient computational techniques, and that we are not able to use a complete atomistic approach. The numerical techniques used in this work are detailed in [Chapter 5](#), while the coarse grained approach we have used to model the dynamics of excited states in a PPV polymer chain is given below.

2.2 The Frenkel-Holstein Model

2.2.1 Frenkel Model

Photo-excitation of polymers typically leads to a linear combination of $\pi \rightarrow \pi^*$ transitions,^[1] resulting in a lone electron that is electrostatically attracted to the positive hole it has created in the π -bonding band. This electron-hole pair, or exciton, can be treated as a quasi-particle, the behaviour of which very much depends on the electron-hole separation. In inorganic systems the separation can be significantly larger than the lattice spacing, giving a Mott-Wannier exciton.^[2] Excitons in π -conjugated polymers, however, can be well modelled by assuming that the electron and hole are tightly bound, and thus that they occupy the same monomer in a polymer chain.^[3] This is the Frenkel exciton,^[1,4] and it is the dynamics of these that we seek to simulate in this work.

In particular, we are interested in the dynamics of Frenkel excitons over many monomers, and not in their behaviour due to their internal structure or when localised on a single monomer. We therefore write the total exciton wavefunction as

$$\Psi_{pj}(r, R) = \phi_p(r)\psi_j(R) \quad (2.2)$$

where r is the electron-hole separation, and R is the Centre of Mass (COM) of the exciton. Thus, $\psi_j(R)$ is the COM wavefunction of the exciton, and $\phi_p(r)$ is the relative electron-hole wavefunction, equivalent to the radial wavefunction for a hydrogenic atom, with p the principal quantum number, and j the COM quantum number. The low dielectric constant of carbon leads to poor screening between the electron and hole, in turn meaning that their root-mean-square separation is on the order of a single monomer. We therefore write

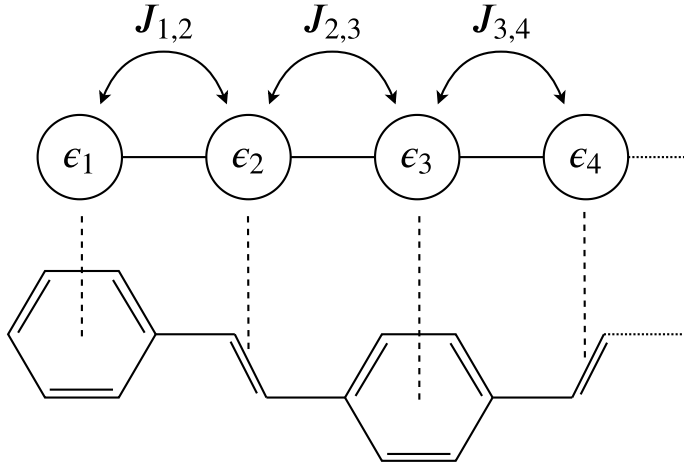


Figure 2.1: *The coarse-graining of a PPV chain.*

$\phi_p(r) = \delta(r, 0)$, such that we only consider Frenkel excitons (and not, for instance, charge transfer excitons, given by $p = 2$). This means that $\psi_j(R)$ is the only component of interest to us for this system, with discrete values of R corresponding to different monomers.

We use the Frenkel Hamiltonian for $\psi_j(R)$ given by

$$\hat{H}_F = \sum_{n=1}^L \epsilon_n \hat{a}_n^\dagger \hat{a}_n + \sum_{n=1}^{L-1} J_n \left(\hat{a}_{n+1}^\dagger \hat{a}_n + \hat{a}_n^\dagger \hat{a}_{n+1} \right), \quad (2.3)$$

where n , the site index, runs over all phenyl- and vinylene-monomers of the chain and $\hat{a}_n^\dagger (\hat{a}_n)$ is the exciton creation (destruction) operator^[5,16] on monomer n .

The first term therefore corresponds to the exciton on-site energies, with ϵ_n being the energy required to create an exciton on an isolated copy of monomer n , containing both the $\pi \rightarrow \pi^*$ energy gap, and the electrostatic stabilisation of the exciton. The number operator $\hat{a}_n^\dagger \hat{a}_n$ counts the number of excitons on monomer n , and therefore this energy only contributes when an exciton is present.

The operator $\hat{a}_{n+1}^\dagger \hat{a}_n$ corresponds to destruction of the exciton on monomer n and creation on monomer $n + 1$ such that the second term allows for the exciton's ability to migrate from monomer n to $n + 1$ and vice versa, where J_n is the exciton transfer integral. There are two possible mechanisms for this process: superexchange (SE) coupling and dipole-dipole (DD) coupling. The former is a through-bond effect, and as such depends on the strength of the wavefunction overlap between neighbouring monomers, giving rise

Parameter	Value	Parameter	Value
J^{SE}	-1.96 eV	J^{DD}	-1.35 eV
E_0	9.24 eV	Δ	3.20 eV
σ_α	65 meV	A	2.0
μ_ϕ	20°	σ_ϕ	15°
$\hbar\omega$	0.2 eV	γ	0.1

Table 2.1: parameter values used in this work

to a $\cos^2(\phi)$ dependence, where ϕ is the torsional angle between neighbouring monomers. The latter is a through space effect, and has a constant contribution, meaning that $J_n = J^{DD} + J^{SE}\cos^2\phi_n$. We have only included nearest neighbour interactions in this work, since the dipole-dipole coupling falls off as $1/r^3$,¹⁷ and hence $J_{n,m}$ falls off as $|n - m|^{-3}$.

For a completely uniform chain, all parameters are uniform such that $\epsilon_n = E_0$ and $J_n = J$, while for an ideal PPV polymer chain the onsite energies alternate, corresponding to phenyl- and vinylene-moieties: $\epsilon_n = E_0 + (-1)^n \frac{\Delta}{2}$ where E_0 is the mean of onsite energies for phenyl- and vinyl-monomers, and Δ is the difference between the two. In physically relevant systems, however, disorder is what leads to interesting behaviour and dynamics in polymers. Onsite energy fluctuations due to local environment density fluctuations give rise to diagonal disorder, while conformational disorder gives rise to off-diagonal disorder; the random distribution of angles between consecutive flat monomers leads to randomly distributed nearest neighbour hopping integrals J_n .

Thus, for a realistic PPV chain, we use:

$$\epsilon_n = E_0 + (-1)^n \frac{\Delta}{2} + \alpha_n, \quad \text{where } \alpha_n \text{ is normally distributed with standard deviation } \sigma_\alpha$$

$$J_n = J^{DD} + J^{SE}\cos^2\phi_n, \quad \text{where } \phi \text{ is normally distributed according to } \sigma_\phi$$

Physically motivated parameter values used in this and previous work¹⁸ are given in Table 2.1.

LEGSS and QEESS

The eigenstates of the Frenkel Hamiltonian for a uniform chain give a discrete approximation to the particle-in-a-box wavefunctions. The introduction of either or both of diagonal and off-diagonal disorder leads to Anderson localisation¹⁹ of these states. This

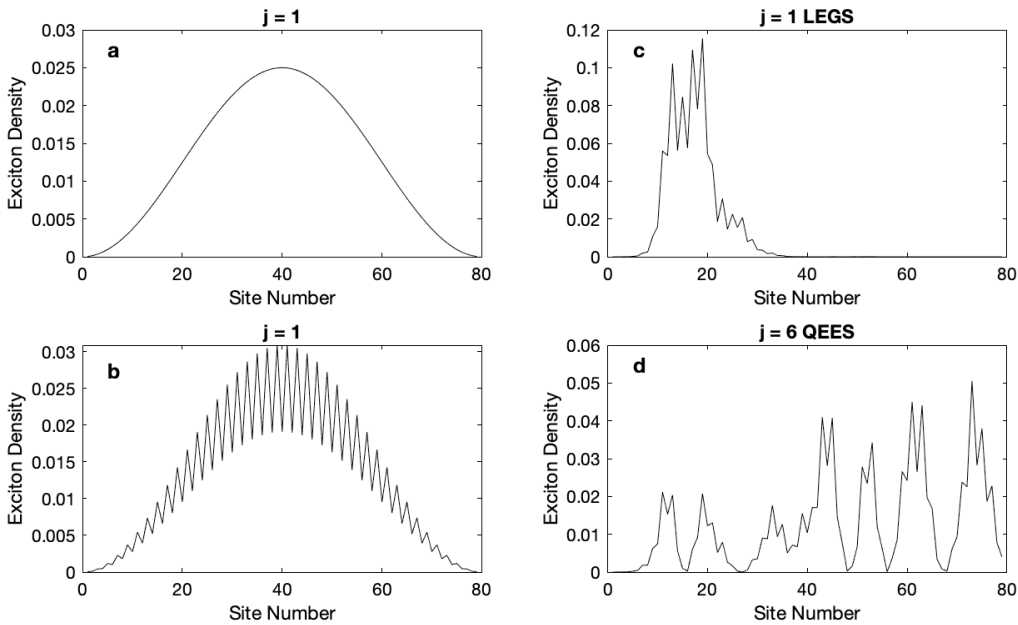


Figure 2.2: The associated exciton density for various 80 moiety chains. (a) corresponds to a uniform, single monomer chain; (b) to a uniform PPV chain; (c) and (d) to a particular conformation of a disordered PPV chain. The COM quantum number, j , is given for each state.

localisation gives rise to several types of eigenstate,⁴ depicted in Figure 2.2:

- **Local Exciton Ground States (LEGSS)** are characterised as being essentially node-less and non-overlapping with each other. It is these which define the chromophores of the system. The signed value parameter

$$\beta = \left| \sum_n |\psi_n| \psi_n \right| \quad (2.4)$$

gives a numerical definition for a LEGS as being $\beta > 0.95$.^{20,21}

- **Quasi-Extended Exciton States (QEESS)** are characterised as spanning multiple LEGSSs, and having at least one node, such that $\beta \sim 0$.
- **Local Exciton Excited States (LEESs)** are less common. They are defined in range by a single LEGS, but have at least one node.

2.2.2 Holstein Model

Exciton-nuclear coupling stabilises excitons, and this coupling is the driving force for the ultrafast dynamics observed in conjugated polymer chains (detailed in Chapter 3).

A classical treatment of the vibrational degrees of freedom is desirable computationally efficient.

ally, since it limits the growth of the Hilbert space dramatically, and has previously been used to model exciton relaxation dynamics in PPV.^{[8][22][23]} Unfortunately, as has been investigated in previous work,^{[24][25]} a classical treatment using the Ehrenfest approximation fails to accurately describe the ultrafast dynamics of interest to us. This is because exciton decoherence, as induced by the exciton-phonon coupling, is absent in the time evolution under this classical approximation. Using this approximation also leads to the unphysical separation of exciton density onto separate chromophores during the relaxation of high-energy states, as seen in *Tozer and Barford*,^[26] meaning that a fully quantised approach to the nuclear degrees of freedom is necessary.

We therefore introduce phonons to the model, represented by isolated simple harmonic oscillators (SHO). We only keep one mode per moiety: the benzenoid-quinoid distortion in the phenylene unit, and C=C double bond stretch in the vinylene unit, meaning that the Frenkel-Holstein Hamiltonian we use is given by^{[26][28]}

$$\hat{H}_{FH} = \hat{H}_F - \frac{A\hbar\omega}{\sqrt{2}} \sum_n \hat{a}_n^\dagger \hat{a}_n (\hat{b}_n^\dagger + \hat{b}_n) + \hbar\omega \sum_n \left(\hat{b}_n^\dagger \hat{b}_n + \frac{1}{2} \right), \quad (2.5)$$

where \hat{b}_n^\dagger (\hat{b}_n) is the SHO raising (lowering) operator on site n , and $\hbar\omega$ is the SHO energy level spacing on both vinylene- and phenylene-monomers. The second term here therefore corresponds to the coupling between the exciton and nuclear vibrations, with the parameter A determining the strength of this coupling, while the last term corresponds to the SHO ladder of energies.

2.3 Open Quantum System

In any isolated quantum system, where all participating degrees of freedom are considered, the observed dynamics are deterministic. That is, if the state of the system at some time is known, together with the Hamiltonian, the state at any other time in the past or future can in principle be known. The time dependence of this state is given by the TDSE, [Equation 2.1](#). For an isolated system, there is no decay, and phase coherence is maintained throughout the dynamics.

No real, physical system is perfectly isolated, however: no matter the definition of

the system, there will always be interactions with external degrees of freedom. These interactions are what cause energy dissipation to the surroundings and phase decoherence to be observed in real systems. In order to accurately describe the dynamics of polymer chains, therefore, the system, defined throughout this work as composing of the excitonic and internal phonon degrees of freedom, needs to be treated as open.

This open quantum system treatment requires a departure from the domain of the TDSE. Several approaches exist to this end,^[29] in this work, we have used the Lindblad master equation^[30]

$$\frac{\partial \rho}{\partial t} = -\frac{i}{\hbar} [\hat{H}_S, \rho] + \gamma \left(\hat{S} \rho \hat{S}^\dagger - \frac{1}{2} \{ \hat{S}^\dagger \hat{S}, \rho \} \right), \quad (2.6)$$

where ρ is the system density matrix, \hat{H}_S is the system Hamiltonian and \hat{S} is the system operator that couples the system to the bath such that the interaction between the two is $\hat{H}_{SB} = \hbar (\hat{S} \hat{B}^\dagger + \hat{S}^\dagger \hat{B})$, where B is an operator acting solely on the bath degrees of freedom.

Inherent in the assumptions^[30,31] of this equation are that the system-bath interaction is weak (i.e that $\tilde{\gamma} = \frac{\gamma}{\omega}$ is small), and that the Markov approximation (that the bath dynamics are rapid and that bath memory effects are short-lived) holds.

In this work, the coupling to the environment is taken to be via vibrational relaxation, such that \hat{S} is the sum over sites of the vibrational lowering operators

$$\hat{S} = \sum_n \hat{b}_n. \quad (2.7)$$

The final form of the master equation is therefore

$$\frac{\partial \rho}{\partial t} = -\frac{i}{\hbar} [\hat{H}, \rho] - \frac{\gamma}{2} \sum_n \left(\hat{b}_n^\dagger \hat{b}_n \rho + \rho \hat{b}_n^\dagger \hat{b}_n - 2 \hat{b}_n \rho \hat{b}_n^\dagger \right), \quad (2.8)$$

where

$$\hat{H} = \hat{H}_{FH} + \frac{\hbar \gamma}{4} \sum_n \left(\hat{Q}_n \hat{P}_n + \hat{P}_n \hat{Q}_n \right). \quad (2.9)$$

This can be further simplified by defining an effective Hamiltonian²²

$$\hat{H}_{\text{eff}} = \hat{H} - \frac{i}{2} \sum_n \hat{b}_n \hat{b}_n^\dagger \quad (2.10)$$

such that

$$\frac{\partial \rho}{\partial t} = -\frac{i}{\hbar} [\hat{H}_{\text{eff}}, \hat{\rho}] + \gamma \sum_n \hat{b}_n^\dagger \rho \hat{b}_n . \quad (2.11)$$

The second term in [Equation 2.10](#) corresponds to the damping correction to the harmonic oscillators.²³ For an oscillator on site n , the dimensionless displacement operator is given by $\hat{Q}_n = \frac{1}{\sqrt{2}} (\hat{b}_n^\dagger + \hat{b}_n)$, and the dimensionless momentum operator by $\hat{P}_n = \frac{i}{\sqrt{2}} (\hat{b}_n^\dagger - \hat{b}_n)$. The choice of the Lindblad operator as the harmonic oscillator destruction operator can thus be justified by noting that the expectation values of these operators have the form of Newton's classical equations of motion for a damped harmonic oscillator:^{24,23}

$$\begin{aligned} \frac{d\langle \hat{Q}_n \rangle}{dt} &= \langle \hat{P}_n \rangle \\ \frac{d\langle \hat{P}_n \rangle}{dt} &= A \langle \hat{a}_n^\dagger \hat{a}_n \rangle - \langle \hat{Q}_n \rangle - \tilde{\gamma} \langle \hat{P}_n \rangle . \end{aligned} \quad (2.12)$$

Chapter 3

Ultrafast Quantum Dynamics

Two ultrafast timescales exist over which, in both physical experiments and quantum simulations,³⁴⁻³⁶ the dynamics of photo-excited states in π -conjugated polymers have been observed. The dynamics corresponding to these timeframes have been analysed in previous work³ using the same theoretical framework as has been presented in Chapter 2, and are detailed below.

3.1 Phonon Energy Transfer

Monitoring the average phonon energy as a function of time after excitation into both a LEGS and a QEES seperately, with and without dissipation is revealing. All four cases show a rapid increase in phonon energy to a maximum within half a vibrational period as seen in Figure 3.1. This corresponds to energy transfer into the internal phonon degrees of freedom and suggests that the initial dynamics are dictated by the Frenkel-Holstein Hamiltonian. Over longer timescales ($> 10\text{fs}$) there is significant decay in the average phonon energy in the open systems ($\gamma \neq 0$). This suggests that the long time scale dynamics are characterised by the non-unitary system-bath interactions.

3.2 Exciton-Polaron Formation

Exciton-polarons are quasi-particles consisting of an exciton which has been “self-trapped” by local displacements of the nuclei. Their presence is clearly shown by the

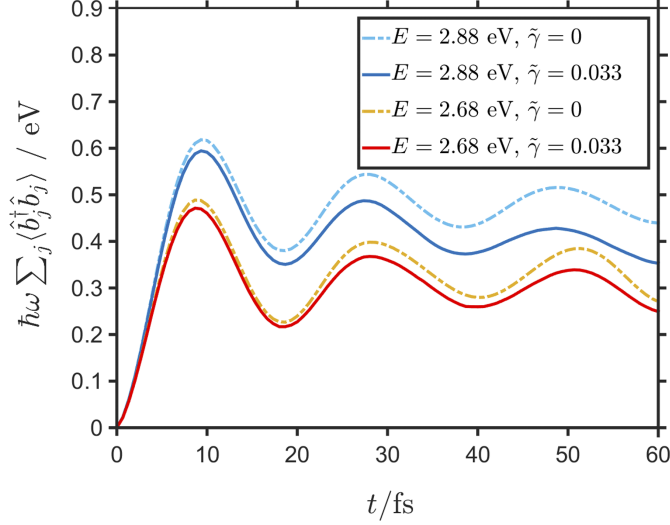


Figure 3.1: Reproduced from *Mannouch et al.*¹

The time dependence of the average phonon energy per site is plotted as a function of time. Dissipation (solid lines) has negligible effect over the short time scales: the first maximum's position is solely a function of $\hbar\omega$. At longer time scales, dissipation leads to decay in the open systems.

exciton-phonon correlation function

$$C_n^{ex-ph} = \frac{1}{A} \sum_m \langle \hat{a}_m^\dagger \hat{a}_m \hat{Q}_{m+n} \rangle , \quad (3.1)$$

which is a measure of the average nuclear displacement n sites away from the exciton. Exciton-polaron formation occurs on an ultrafast timescale of half a vibrational period (10 fs) of the SHOs, and corresponds to a rapid initial growth in this correlation function, with persisting oscillations at the vibrational period. The only parameter in the model which affects the time of this formation is the vibrational period, $\hbar\omega$.

3.3 Exciton Decoherence

In general it is possible for excitons to display long range quantum coherences between different monomers and, over ultrashort time frames, these can span many chromophores. A suitable measure of the magnitude of the exciton coherences is from the off-diagonal elements of the exciton reduced density matrix,² which is obtained by tracing over the nuclear degrees of freedom

$$\rho_{ex} = \sum_v \langle v | \rho | v \rangle . \quad (3.2)$$

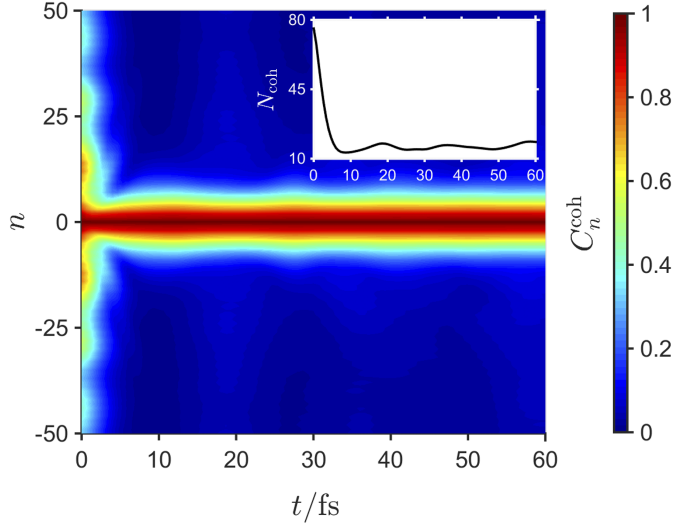


Figure 3.2: Reproduced from *Mannouch et al.*^[4]

A plot of C_n^{ex-ph} as a function of n and t . Long range coherences are present upon initial excitation. The range of these rapidly decay in time. The inset shows the time dependence of the coherence number, N_{coh} .

The correlation function

$$C_n^{coh} = \sum_m |\langle m | \rho_{ex} | m + n \rangle| \quad (3.3)$$

is therefore a measure of the average magnitude of the coherence between exciton amplitude n monomers apart, such that the coherence number $N_{coh} = \sum_n C_n^{coh}$ is a measure of the average coherence length.

It can be seen from Figure 3.2 that these exciton-site coherences rapidly decay in time. This can be rationalised by first noting that the total wavefunction can be written in the basis $|\psi\rangle = \sum_n \psi_n |n\rangle |V_n\rangle$, such that ψ_n is the probability amplitude of the Frenkel exciton residing on monomer n with the L harmonic oscillators described by $|V_n\rangle$. In this representation, C_n^{coh} can be rewritten as

$$C_n^{coh} = \sum_m = |\psi_m \psi_{m+n}^* \langle V_{m+n} | V_n \rangle| . \quad (3.4)$$

The rapid decay in coherence length therefore stems from the decay in the overlap $\langle V_{m+n} | V_n \rangle$ seen due to exciton-polaron formation.

Therefore, this process again depends on the vibrational energy $\hbar\omega$, but also on the exciton-phonon coupling parameter A : a larger value of A leads to more rapid decay in

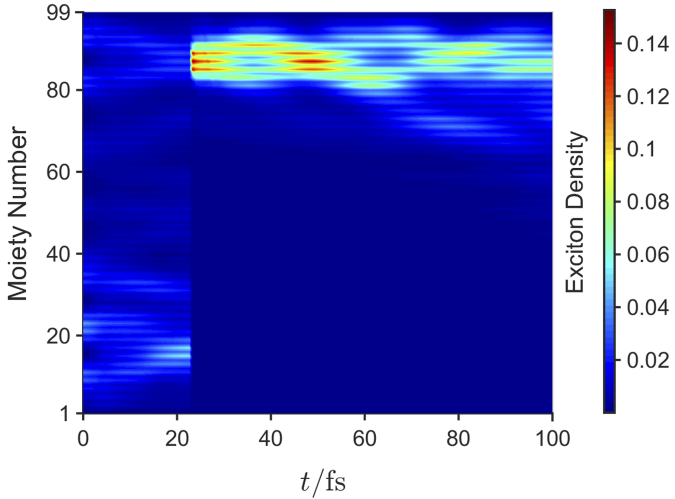


Figure 3.3: Reproduced from *Mannouch et al.*⁹

The time evolution of the exciton density. The system-bath interaction (quantum jump) at $t \sim 25$ fs leads to wavefunction collapse, and localisation onto a single chromophore.

the coherences as a function of both t and n , since it gives rise to increased vibrational displacements, and thus a quicker decay in vibrational overlaps.

3.4 Exciton Localisation

Despite the rapid decay in range of exciton coherences within the first vibrational period, the exciton density can still be delocalised over large regions of the chain for significantly longer times. The time scale over which the exciton density localises is determined by the external dissipation parameter γ , and its mechanism is that of wavefunction collapse: the local environment interactions act as a form of quantum measurement. Hence, by removing a quantum of vibrational energy from monomer n , only states of the harmonic oscillator at n with non-zero displacement are kept. The correlation between nuclear displacement and the exciton mean that the exciton localises onto the chromophore that contains site n . This localisation can be observed in Figure 3.3, where a bath-system interactions occurs at ~ 25 fs.

Chapter 4

Theory of Spectroscopy

Spectroscopy is the study of the interaction between light and matter, and is one of the fundamental exploratory tools available to experimentalists in all sciences. Different spectroscopies range over many energy scales, with varying degrees of conceptual complexity.

In this chapter, we begin by presenting the form of a one-dimensional absorption spectrum. The key concept in this description is the interpretation of the spectrum as a Fourier transform of the time dependent overlap $\langle \Psi(0) | \Psi(t) \rangle$.

We then introduce the technique used in this work: two dimensional electronic coherence spectroscopy. The dynamics along specific pathways of system-light interactions are of interest to us, and are again captured in a time dependent overlap. We present a theory of these interactions, the results of which can be used to justify an experimental procedure for isolating specific contributions to the total time signal measured.

4.1 Linear Absorption Spectroscopy

A general expression for the absorption of a quantum system is^{87,88}

$$F(E) = aE \int_0^\infty e^{iEt} \langle \Psi(0) | \Psi(t) \rangle dt , \quad (4.1)$$

where a is a known constant, energies E are relative to the ground state, $\langle \Psi(0) | \Psi(t) \rangle$ is the autocorrelation function of the wavefunction upon excitation from the ground state, with $|\Psi(0)\rangle = \hat{\mu} |\Psi_{GS}\rangle$, and $\hat{\mu}$ is the electronic dipole operator.

For an isolated system initially in the ground state

$$|\Psi(t)\rangle = \sum_n c_n e^{-iE_n t} |\psi_n\rangle , \quad (4.2)$$

where $c_n = \langle\psi_n| \hat{\mu} |\Psi_{GS}\rangle$ and $\{|\psi_n\rangle\}$ are the eigenstates of the Hamiltonian; these can be written as a product of electronic and nuclear parts $|\psi_n\rangle = |\psi_n^{el}\rangle |\chi_n\rangle$, giving $c_n = \langle\psi_n^{el}| \hat{\mu} |\psi_{GS}^{el}\rangle \langle\chi_n|\chi_{GS}\rangle$.

This system therefore has a spectrum given by

$$\begin{aligned} F(E) &= aE \int_0^\infty e^{iEt} \sum_{n,m} c_m^* c_n e^{i(E_m - E_n)t} \langle\psi_m|\psi_n\rangle dt \\ &= aE \sum_n |c_n|^2 \delta(E - E_n) . \end{aligned} \quad (4.3)$$

The form of this is a stick spectrum: an array of delta-peaks is observed at eigenenergies $\{E_n\}$ corresponding to the difference between excited states $\{|\psi_n\rangle\}$ and the ground state $|\Psi_{GS}\rangle$, with amplitudes $|c_n|^2$ dictated by the electronic selection rule and the Franck-Condon overlap.^[10]

For a system in which excited state populations decay, $|\psi(t)\rangle = \sum_n c_n e^{-iE_n t} e^{-\gamma_n t} |\psi_n\rangle$, the form of the spectrum is now a sum of complex valued Lorentzians:

$$\begin{aligned} F(E) &= aE \int_0^\infty |c_n|^2 e^{i(E - E_n)t - \gamma_n t} dt \\ &= aE \sum_n \frac{|c_n|^2}{\gamma_n - i(E_n - E)} . \end{aligned} \quad (4.4)$$

Relaxation dynamics of excited states can thus be partially explored using one dimensional spectroscopy; in this case the linewidth of the peak corresponds to the lifetime of the excited state.

4.2 Two-Dimensional Electronic Coherence Spectroscopy

While linear spectroscopies can be used to probe the dynamics of systems, their single frequency dimension limits their scope. Two dimensional spectroscopies provide a means for much deeper analysis of dynamics.^{[1]-[4]}

Typically, two- and higher-dimensional spectroscopies involve a series of $n+1$ pulses,

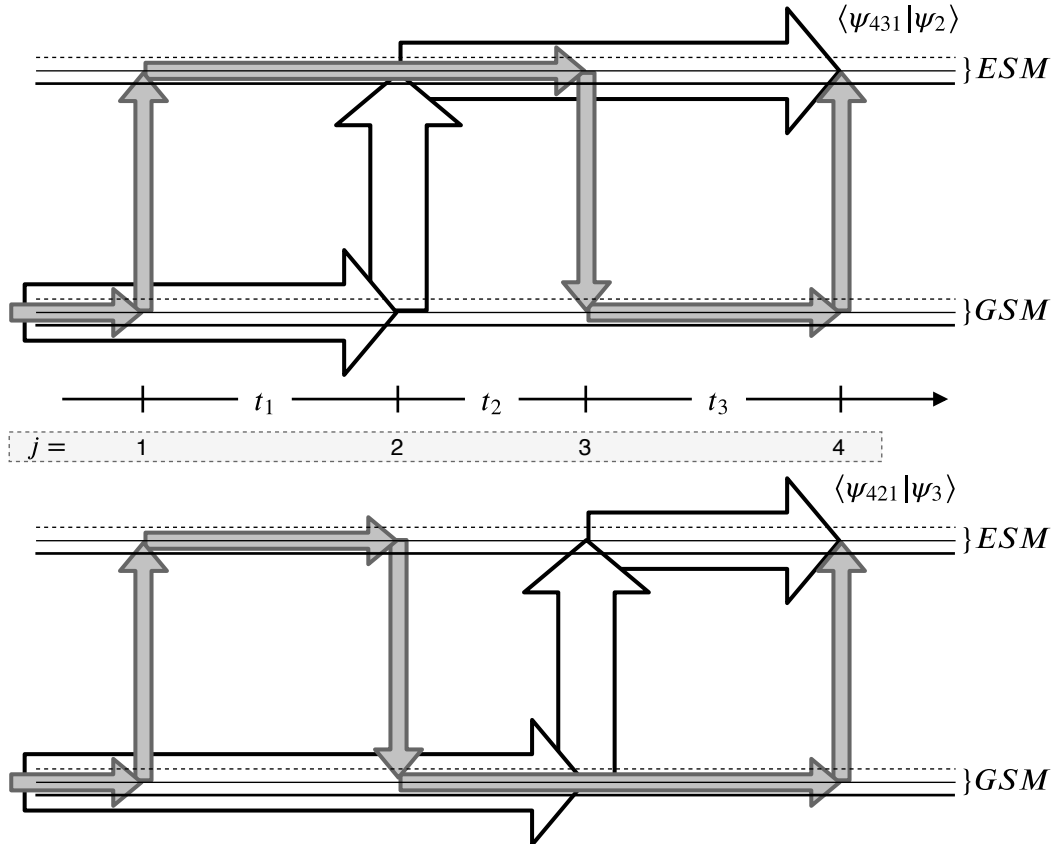


Figure 4.1: The two pathways are of interest. In both, one pulse excites a first order wavepacket ($|\psi_2\rangle$ and $|\psi_3\rangle$) from the ground state to the Excited State Manifold (ESM). The other three pulses excite a third order wavepacket ($|\psi_{431}\rangle$ and $|\psi_{421}\rangle$ respectively) from the ground state into the ESM, before enabling a groundstate mediated transition back to the ESM.

The first order wavepackets are represented by white arrows, and the third order wavepackets by the grey arrows. Vertical arrows represent laser action. Horizontal arrows represent wavepacket evolution in the corresponding manifold. Similar diagrams have been by Tekavec *et al.*³⁹ and by Apkarian *et al.*⁴⁰ to describe resonance Raman experiments. These are similar in spirit to double-sided Feynman diagrams, detailed in section 4.3

t_j represents the time interval between pulses j and $j + 1$.

separated by well defined time intervals. Scanning over each of these n time intervals provides up to another n dimensions to the signal and thus to the spectrum. The pulse sequence for two dimensional electronic coherence spectroscopy (2D ECS) is basic:^{39,43} four sequential pulses directed at the sample arrive at times $t^{(1)}, t^{(2)}, t^{(3)}$ and $t^{(4)}$. Specific contributions to the third order response, proportional to the excited state population,³⁹ are measured as a function of the three time delays, given by $t_j = t^{(j+1)} - t^{(j)}$ for $j \in 1, 2, 3$. A Fourier transform with respect to t_1 , the coherence time, and t_3 , the echo time, for fixed t_2 , the waiting time, gives the 2D ECS spectrum.

Many system-light interactions are possible with this pulse sequence; in 2D ECS, we isolate the signal, as evaluated directly after the last pulse, corresponding to the excited state terms produced when the bra of the system density operator is excited by the second or third pulse, and when the ket undergoes excitation, de-excitation and re-excitation due to interaction with the remaining three pulses (and vice versa). These contributions ($\langle\psi_{431}|\psi_2\rangle$ and $\langle\psi_{421}|\psi_3\rangle$) are illustrated in Figure 4.1, and allow us to explore the coherences and couplings between different optical modes.

We present below a description of the theory underpinning light-matter interactions that allows us to understand how these specific pathway contributions can be isolated experimentally. Typically, third order response theory is used in this context, but instead we use a more intuitive, yet ultimately equivalent, wave-packet description, a more detailed account of which can be found in *Tekavec et al.*³⁹

4.2.1 Wave-Packet Analysis

The Hamiltonian for the system of interest can be written as

$$\hat{H}(t) = \hat{H}_0 + \hat{V}(t) , \quad (4.5)$$

where \hat{H}_0 describes the system in the absence of light, and $\hat{V}(t)$ introduces the perturbation due to the electric field. Using the dipole approximation, we can write this perturbation as

$$V(t) = -\hat{\mu} \cdot \underline{E}(t) , \quad (4.6)$$

where the transition dipole operator $\hat{\mu}$ couples states

$$\underline{\hat{\mu}} = \sum_{n,m} |n\rangle \underline{\mu_{n,m}} \langle m| . \quad (4.7)$$

The total electric field of the pulse train can be written as a sum of the four individual pulses, labelled $j \in \{1, 2, 3, 4\}$, such that

$$\underline{E}(t) = \sum_{j=1}^4 \underline{E}_j(t - t^{(j)}) . \quad (4.8)$$

where $t^{(j)}$ is the time that the centre of pulse j reaches the system.

Using first order perturbation theory we can write⁴⁵

$$|\psi_j(t)\rangle = -i \int_0^t e^{-i\hat{H}_0(t-t')} \hat{V}_j(t' - t^{(j)}) e^{-i\hat{H}_0 t'} |0\rangle dt' , \quad (4.9)$$

where $|\psi_j(t)\rangle$ is the first-order excited state contribution caused by interaction with pulse j . Reading this equation from right to left gives an intuitive interpretation of the origin of this first-order excited state contribution: the system evolves in its ground state, $|0\rangle$, for a time t' , before the perturbation, centred at $t^{(j)}$, is applied. This instantaneously creates excited state amplitude, which then evolves for a further time $(t - t')$. The time at which the interaction occurs, t' , is integrated over, but by assuming that the electric field of the laser pulse is described by a δ -function, this interpretation is exact in that only the pathway corresponding to $t' = t^{(j)}$ contributes to the first-order excited state contribution.

As detailed in [Chapter 5](#), this is exactly how we calculate $|\psi_j\rangle$.

Thus, writing $\underline{\hat{\mu}} \cdot \underline{E}_j(t' - t^{(j)}) = A_j \hat{\mu} \delta(t' - t^{(j)}) e^{i\phi_j}$ gives

$$\begin{aligned} |\psi_j(t)\rangle &= i A_j e^{i\phi_j} \int_{-\infty}^{\infty} e^{-i\hat{H}_0(t-t')} \hat{\mu} \delta(t' - t^{(j)}) e^{-i\hat{H}_0 t'} |0\rangle dt' \\ &= i A_j e^{i\phi_j} \sum_{a,b} e^{-i\hat{H}_0(t-t^{(j)})} |a\rangle \mu_{ab} \langle b|0\rangle \\ &= i A_j e^{i\phi_j} \sum_a e^{-iE_a(t-t^{(j)})} \mu_{ao} |a\rangle . \end{aligned} \quad (4.10)$$

where A_j is a function of the laser intensity and direction, ϕ_j is the phase of the laser pulse, E_a is the energy of eigenstate $|a\rangle$ relative to the ground state, and the integral limits can be expanded to $(-\infty, \infty)$ due to the narrow nature of the pulse.

Similarly, the third-order contributions to the excited state amplitude are given by

$$|\psi_{mlk}(t)\rangle = (-i)^3 \int_0^t dt' \int_0^{t'} dt'' \int_0^{t''} dt''' e^{-i\hat{H}_0(t-t')} \hat{V}_m(t' - t^{(m)}) e^{-i\hat{H}_0(t'-t'')} \\ \times \hat{V}_l(t'' - t^{(l)}) e^{-i\hat{H}_0(t''-t''')} \hat{V}_k(t''' - t^{(k)}) e^{-i\hat{H}_0 t'''} |0\rangle . \quad (4.11)$$

Assuming again that the pulses are δ -functions, and further that the interactions are well separated in time (such that $m > l > k$), means that this reduces to

$$|\psi_{mlk}(t)\rangle = -iA_m A_l A_k e^{i(\phi_m - \phi_l + \phi_k)} \sum_{a,b} \mu_{a0} \mu_{b0}^2 e^{-i\omega_{a0}(t-t^{(m)})} e^{-iw_{b0}(t^{(l)}-t^{(k)})} |a\rangle , \quad (4.12)$$

where the negative sign of ϕ_l corresponds to de-excitation from the excited state manifold, and where we have further assumed here that all transitions involve either excitation to or de-excitation from the ground state. Under this assumption, only odd order wavepackets contain excited state amplitude. Ignoring higher order interactions therefore gives a total excited state contribution of

$$|\psi_{ex}(t)\rangle = \sum_{j=1}^4 |\psi_j(t)\rangle + \sum_{m>l>k=1}^4 |\psi_{mlk}(t)\rangle , \quad (4.13)$$

and therefore the excited state population is given by

$$\langle \psi_{ex}(t) | \psi_{ex}(t) \rangle = \sum_{j',j} \langle \psi_j(t) | \psi_{j'}(t) \rangle \\ + \sum_{\substack{m \geq l \geq k, \\ j}} \langle \psi_j(t) | \psi_{mlk}(t) \rangle + \langle \psi_{mlk}(t) | \psi_j(t) \rangle \\ + \sum_{\substack{m \geq l \geq k, \\ m' \geq l' \geq k'}} \langle \psi_{m'l'k'}(t) | \psi_{mlk}(t) \rangle . \quad (4.14)$$

To calculate a 2D ECS spectrum, we are interested in the terms $\langle \psi_{431} | \psi_2 \rangle$ and $\langle \psi_{421} | \psi_3 \rangle$, evaluated at the time of the fourth pulse. Separating these from all other terms is possible by measuring the third order polarisability, which is proportional to the excited state population.⁸⁹

1. We note that in Equation 4.14 the three sets of terms are, respectively, linear, quadratic and cubic with respect to the laser intensity. Thus we can isolate $\langle \psi_j | \psi_{mlk} \rangle + \langle \psi_{mlk} | \psi_j \rangle = 2\text{Re} \langle \psi_{mlk} | \psi_j \rangle$ from the fluorescence signal.
2. Each interaction leads to addition of the pulse phase onto the total phase of the

wavefunction. By further isolating contributions which are linear with respect to each of the four laser pulse phases, we are left with $2\text{Re} \sum_{m \neq l \neq k \neq j} \langle \psi_{mlk} | \psi_j \rangle$. These are: $\langle \psi_{432} | \psi_1 \rangle$, $\langle \psi_{431} | \psi_2 \rangle$, $\langle \psi_{421} | \psi_3 \rangle$ and $\langle \psi_{321} | \psi_4 \rangle$

3. Finally, the non-rephasing and rephasing contributions can be isolated by noting that $\langle \psi_{432} | \psi_1 \rangle$ and $\langle \psi_{321} | \psi_4 \rangle$ oscillate with factor $e^{i[(\phi_4 - \phi_3) + (\phi_2 - \phi_1)]}$ (non-rephasing) while the terms $\langle \psi_{431} | \psi_2 \rangle$ and $\langle \psi_{421} | \psi_3 \rangle$ oscillate according to $e^{i[(\phi_4 - \phi_3) - (\phi_2 - \phi_1)]}$ (rephasing).

4.2.2 Experimental Setup

Experimentally, the precise control of times and phases needed to measure this time signal is challenging. A simplified overview of one method to achieve this is given below, with a full account being available from *Tekavec et al.*^[39]

A mode-locked laser is used to produce an ultrashort (fs) pulse containing frequencies to resonantly excite wavepackets from the ground state manifold to the excited state manifold (i.e. $\alpha(\omega) \neq 0$ for the transitions to states of interest).

This pulse is split into the four pulses necessary using two layers of 50:50 beam splitters. As above, we label these pulses with $j \in \{1, 2, 3, 4\}$. Two paired sets of Acousto-Optic Bragg Cells operating at distinct frequencies, Ω_{21} and Ω_{43} , are used to impart a relative phase shift $\phi_{21} = \phi_2 - \phi_1$ between pulses 1 and 2, and ϕ_{43} between 3 and 4, such that $\phi_{21} = \Omega_{21}t'$ where t' is the lab frame time. Thus for a time $\Delta t' = T$ between pulse trains, the relative phase ϕ_{21} advances by $\Omega_{21}T$. The inter-pulse delays within the train are controlled by controlling the path length of the pulses.

By creating suitable reference signals,^[39] the phase of the third order polarisability, and therefore that of the excited state contributions, can be measured. The total time signal for a single co-ordinate in (t_1, t_2, t_3) -space is therefore built up by fixing the inter pulse delays and taking many consecutive measurements spaced a time T apart, effectively scanning over a complete cycle of $\phi_{43} + \phi_{21}$. The overlaps $\langle \psi_{431} | \psi_2 \rangle$ and $\langle \psi_{421} | \psi_3 \rangle$ can be extracted by isolating the complex amplitude of the signal oscillating at $\phi_{43} - \phi_{21}$.

This process is repeated for all co-ordinates of interest in the space spanned by t_1, t_2

and t_3 . Typically, this means that for a few fixed values of the waiting time t_2 , both t_1 and t_3 are scanned over with increment Δt and range $T = N\Delta t$.

4.2.3 The Spectrum

In the literature, several alternative representations of the 2D ECS spectrum exist. The purely absorptive spectrum is given by

$$\text{Re} (\mathcal{F} [\langle \psi_{431} | \psi_2 \rangle + \langle \psi_{421} | \psi_3 \rangle + \langle \psi_{432} | \psi_1 \rangle + \langle \psi_{321} | \psi_4 \rangle]) , \quad (4.15)$$

i.e., the real part of the Fourier transform of the sum of all four first-order third-order coherences.

An alternative representation is

$$\text{Abs} (\mathcal{F} [\langle \psi_{431} | \psi_2 \rangle + \langle \psi_{421} | \psi_3 \rangle]) , \quad (4.16)$$

i.e., the absolute value of the Fourier transform of the rephasing time signals. The purely absorptive spectrum gives slightly reduced peak widths, but otherwise provides the same information as this spectrum.⁴³

Experimentally it is not possible to separate contributions to the signal detected from the pathways $\langle \psi_{431} | \psi_2 \rangle$ and $\langle \psi_{421} | \psi_3 \rangle$. In our simulations, it is possible to do so, however. For $t_2 = 0$ it can be noted that $\langle \psi_{431} | \psi_2 \rangle = \langle \psi_{421} | \psi_3 \rangle$. The t_2 behaviour of $\langle \psi_{431} | \psi_2 \rangle$ corresponds to joint evolution in the excited state manifold, while that of $\langle \psi_{421} | \psi_3 \rangle$ corresponds to joint evolution in the ground state manifold. Since we are interested in the exciton dynamics in this work, we have used

$$\text{Abs} (\mathcal{F} [\langle \psi_{431} | \psi_2 \rangle]) \quad (4.17)$$

as the representation of the 2D ECS spectrum.

4.3 Double-sided Feynman Diagrams

The standard language of non-linear spectroscopy is the double-sided Feynman diagram (DSFD).^{42,43} These are similar in spirit to the diagram we present in [Figure 4.1](#), and we make use of one in the analysis of the spectra in [Chapter 7](#). We therefore briefly detail

their interpretation below, a more thorough description for a more general electric field can be found in *Hamm and Zanni*.⁴³

The two vertical lines represent the time evolution of the ket and bra (left and right lines respectively) of the system density matrix, with time running upwards. Interactions with light through the transition dipole operator are represented by arrows; stimulated absorption corresponds to an arrow pointing inwards, while stimulated emission corresponds to an arrow pointing outwards. During periods of evolution, the corresponding matrix-element is written between the vertical lines, and this rotates at the difference in energy between the bra and ket.

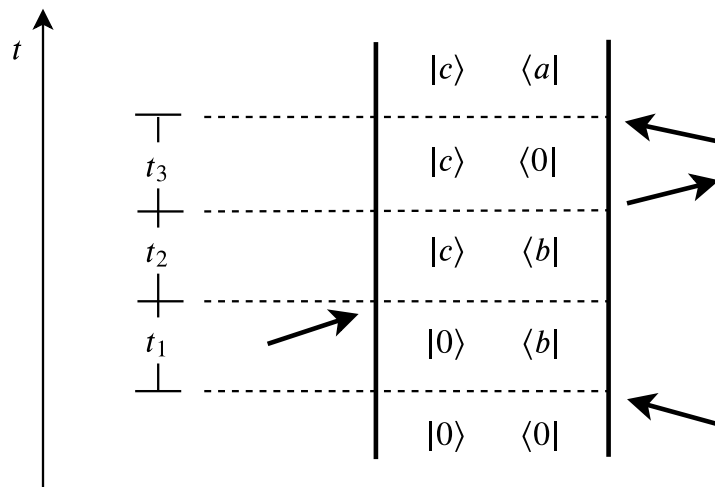


Figure 4.2: a double sided Feynman diagram, corresponding to $\langle\psi_{431}|\psi_2\rangle$ as in Equation 4.10 and Equation 4.12.

Chapter 5

Computational Methods

In order to calculate the time signal $\langle \psi_{431} | \psi_2 \rangle$, we need to be able to both evolve the system in time, and simulate the effect on the system of interactions with light. Even for our coarse grained model, the complete Hilbert space is too large to work with in a complete sense. We therefore need an efficient means to truncate the system without a significant loss in accuracy.

In this work, we have used the Tensor Network Theory Library^[4] to simulate the dynamics of the system, according to the Lindblad master equation, using the TEBD scheme; I have modified this to be able to measure wavefunction overlaps as a function of the three time delays t_1 , t_2 , and t_3 , and I have devised a scheme to sample $\langle \psi_{431} | \psi_2 \rangle$ over these three time dimensions efficiently

5.1 System Representation and Evolution

5.1.1 TEBD

Time-evolving block decimation (TEBD) is a numerical technique used to efficiently simulate the quantum dynamics of one-dimensional systems where at most nearest-neighbour interactions are considered.^[47-49] It is of particular use when the overall entanglement of the system is low, and hence is a good choice as a scheme to use in this work.

The scheme relies on the assumption that the interesting, relevant and low energy quantum dynamics of a system take place in a greatly reduced subspace of the complete Hilbert space. By evolving the system in time and dynamically identifying this subspace, states

of no interest can be discarded, giving an exponentially large decrease in calculation times for both the system density matrix, and the calculations of any observables. Indeed, the computation time scales linearly, rather than exponentially, with the number of sites.^[47,49] While a complete description of the procedure is beyond the scope of this thesis, a brief summary is given below.

Any pure quantum state composing of many particles can be written as

$$|\psi\rangle = \sum_{\sigma_1, \dots, \sigma_L}^d c_{\sigma_1, \dots, \sigma_L} |\sigma_1, \dots, \sigma_L\rangle, \quad (5.1)$$

where there exists a d -dimensional local state space $\{\sigma_i\}$ on each of the L sites. This gives an exponentially growing number of coefficients, with each $c_{\sigma_1, \dots, \sigma_L}$ a rank- L Tensor.

In our particular case there are $(2(n_{max} + 1))^L$ states, and therefore coefficients, where L is the length of the chain, and n_{max} the highest vibrational quantum number considered for the harmonic oscillator on each site. Considering 20 sites, and 3 vibrational levels gives $\sim 3 \times 10^{15}$ coefficients.

In one dimension, an alternative description is via a matrix product state (MPS)^[50]

$$|\psi\rangle = \sum_{\sigma_1, \dots, \sigma_L} A^{\sigma_1} A^{\sigma_2} \dots A^{\sigma_{L-1}} A^{\sigma_L} |\sigma_1, \dots, \sigma_L\rangle, \quad (5.2)$$

where the matrices A^{σ_i} are found by the Schmidt decomposition of $c_{\sigma_1, \dots, \sigma_L}$. An exact description does not reduce the system size. A single value decomposition can be used to great effect, however: it is what allows the determination of the matrices A^{σ_n} for a general system, but also gives a measure of the importance of each state (the singular values) as the MPS is built up. By limiting the internal dimensions of the matrices to be less than or equal to some parameter χ , an exponentially simpler description of the system can be given, with very little loss in accuracy. This is the Schmidt decomposition.

Furthermore, the numerical value for the error in this description can be easily evaluated as the sum of singular values corresponding to discarded states. In this work, we have used an internal truncation parameter $\chi = 80$, with the total error of the procedure being kept to less than 1 in 10^3 .

5.1.2 Trotter Decomposition

To simulate quantum dynamics, one must have a quantum evolution operator, $e^{-i\hat{H}\delta t}$. For systems occupying large Hilbert spaces, this is not computationally possible. The Trotter decomposition⁵¹ is used within the TEBD technique to side step this issue, by expanding the evolution operator: for systems containing only on-site and nearest neighbour terms, as is the case here, the Hamiltonian can be written as

$$\hat{H} = \sum_{n=1}^{L-1} \hat{H}_{n,n+1}, \quad (5.3)$$

where the interpretation of $\hat{H}_{n,n+1}$ is as the Hamiltonian for the “bond” between adjacent sites n and $n + 1$. Using this, the Trotter decomposition for the evolution operator is

$$e^{-i\hat{H}\delta t} \simeq e^{-\frac{i}{2}\hat{H}_{1,2}\delta t} e^{-\frac{i}{2}\hat{H}_{2,3}\delta t} \dots e^{-\frac{i}{2}\hat{H}_{2,3}\delta t} e^{-\frac{i}{2}\hat{H}_{1,2}\delta t} + O(\delta t^3). \quad (5.4)$$

The error $O(\delta t^3)$ becomes negligible for short enough time intervals and hence, in this work, we have used dimensionless time intervals ($\Delta\tilde{t} = \omega\Delta t$) of 0.005.

5.1.3 Quantum Jumps

The quantum jump trajectory method facilitates the computational simulation of a system governed by the Lindblad master equation⁵² (Equation 2.8). The system is allowed to evolve as governed by \hat{H}_{eff} (Equation 2.10), and experiences quantum jumps at random times, the rate of which is governed by γ . Many jump trajectories are taken, and averaging over these is equivalent to evaluating the density operator as described by the Lindblad master equation.

To evolve a system for a total time T , one must first split this time into many small timesteps: $N\delta t = T$. The effective Hamiltonian from Equation 2.10 gives us a step evolution operator: $e^{-i\hat{H}_{\text{eff}}\delta t}$. Taking an initial state and evolving it gives a trial state at a time $t + \delta t$:

$$|\psi_{\text{trial}}(t + \delta t)\rangle = e^{-i\hat{H}_{\text{eff}}\delta t} |\psi(t)\rangle. \quad (5.5)$$

The effective Hamiltonian is non-Hermitian, and hence this evolution does not conserve

the state's norm,

$$\langle \psi_{\text{trial}}(t + \delta t) \rangle | \psi_{\text{trial}}(t + \delta t) \rangle = 1 - \delta p . \quad (5.6)$$

The state of the wavefunction at $t + \delta t$ is then determined stochastically:

with probability $1 - \delta p$:

$$| \psi(t + \delta t) \rangle = \frac{| \psi_{\text{trial}}(t + \delta t) \rangle}{\sqrt{1 - \delta p}} ; \quad (5.7)$$

the trial state is renormalised. Or, with probability δp :

$$| \psi(t + \delta t) \rangle = \frac{\hat{b}_n | \psi(t) \rangle}{\sqrt{\langle \psi(t) | \hat{b}_n^\dagger \hat{b}_n | \psi(t) \rangle}} ; \quad (5.8)$$

one of the vibrational lowering operators is applied to the system before renormalisation, giving a “quantum jump”. n is also chosen stochastically, with probability

$$P_n = \frac{\langle \psi(t) | \hat{b}_n^\dagger \hat{b}_n | \psi(t) \rangle}{\sum_m \langle \psi(t) | \hat{b}_m^\dagger \hat{b}_m | \psi(t) \rangle} . \quad (5.9)$$

Computationally, this is equivalent to calculating $| \psi_{\text{trial}}(t + \delta t) \rangle$. If a randomly generated number is less than δp , one applies the jump operator to $| \psi(t) \rangle$ otherwise $| \psi_{\text{trial}}(t + \delta t) \rangle$ is kept. The wavefunction is then normalised.

5.2 System-Light Interactions

As in [Equation 4.10](#) and [Equation 4.12](#), we have

$$\begin{aligned} | \psi_2(t_1, t_2, t_3) \rangle &= iA \sum_a \mu_{a,0} \cdot e^{-iE_a(t_2+t_3)} \cdot e^{i\phi_2} | a \rangle ; \\ | \psi_{431}(t_1, t_2, t_3) \rangle &= -iA^3 \sum_{a,b} \mu_{a,0} \mu_{b,0}^2 \cdot e^{-iE_b(t_1+t_2)} \cdot e^{-i(\phi_m-\phi_l+\phi_k)} | a \rangle \end{aligned}$$

or equivalently

$$\begin{aligned} | \psi_2(t_1, t_2, t_3) \rangle &= \hat{U}(t_2 + t_3) \cdot \hat{O} | GS \rangle \\ | \psi_{431}(t_1, t_2, t_3) \rangle &= \hat{O} \cdot \hat{U}(t_3) \cdot \hat{O}^\dagger \cdot \hat{U}(t_1 + t_2) \cdot \hat{O} | GS \rangle , \end{aligned} \quad (5.10)$$

where $\hat{U}(t)$ is the evolution operator for a time t , and \hat{O} (\hat{O}^\dagger) is the excitation (de-excitation) operator. Experimentally, the pulse phases ϕ_n imparted on the timesignal are used to ex-

tract the overlaps of interest from the total time signal. We disregard these phases imparted by \hat{O} here, since we can calculate the overlap $\langle \psi_{431} | \psi_2 \rangle$ directly.

Looking at these results further, we can see that the effect of the light, \hat{O} , is to excite the system into a linear combination of excited states, determined by the absorption strength $\mu_{0,a}$. It is assumed that these transitions are vertical, i.e., that the nuclei are frozen on the timescale of the excitation. This is the Franck-Condon approximation.¹⁰ The amplitude of the exciton in the site basis is therefore given by a linear combination of eigenstates of the Frenkel Hamiltonian. We control this combination by supplying a coefficient for the exciton density on each site to the excitation operator \hat{O} . The populations of the vibrational states are then calculated based upon their Franck-Condon overlap with the vibrationally cold ground state, such that they depend solely on the exciton-phonon coupling parameter A .

Typically polymers only absorb strongly into a few of the lowest energy eigenstates of the Frenkel Hamiltonian.⁹ Absorption into other states does not vanish, but has assumed to do so in this work to avoid the effects of undersampling detailed in [Figure 6.1](#), and to produce uncongested and easily interpretable spectra.

5.3 Efficient Time Signal Calculation

We need to calculate $\langle \psi_{431} | \psi_2 \rangle$ as a function of the three time variables t_1 , t_2 and t_3 . Specifically, we would like to take two dimensional discrete Fourier transforms with respect to the coherence time, t_1 , and echo time, t_3 , for several values of the waiting time, t_2 . As detailed in [Chapter 6](#), we therefore need to take up to 400 data points in each of t_1 and t_3 for each value of interest of the waiting time, t_2 .

To efficiently sample all these data points, I have developed the following schemes for the isolated and open system cases respectively.

5.3.1 Isolated Case

Experimentally, suitably long times are left between each pulse train such that the system returns to the ground state. Directly mimicking this computationally, by calculating

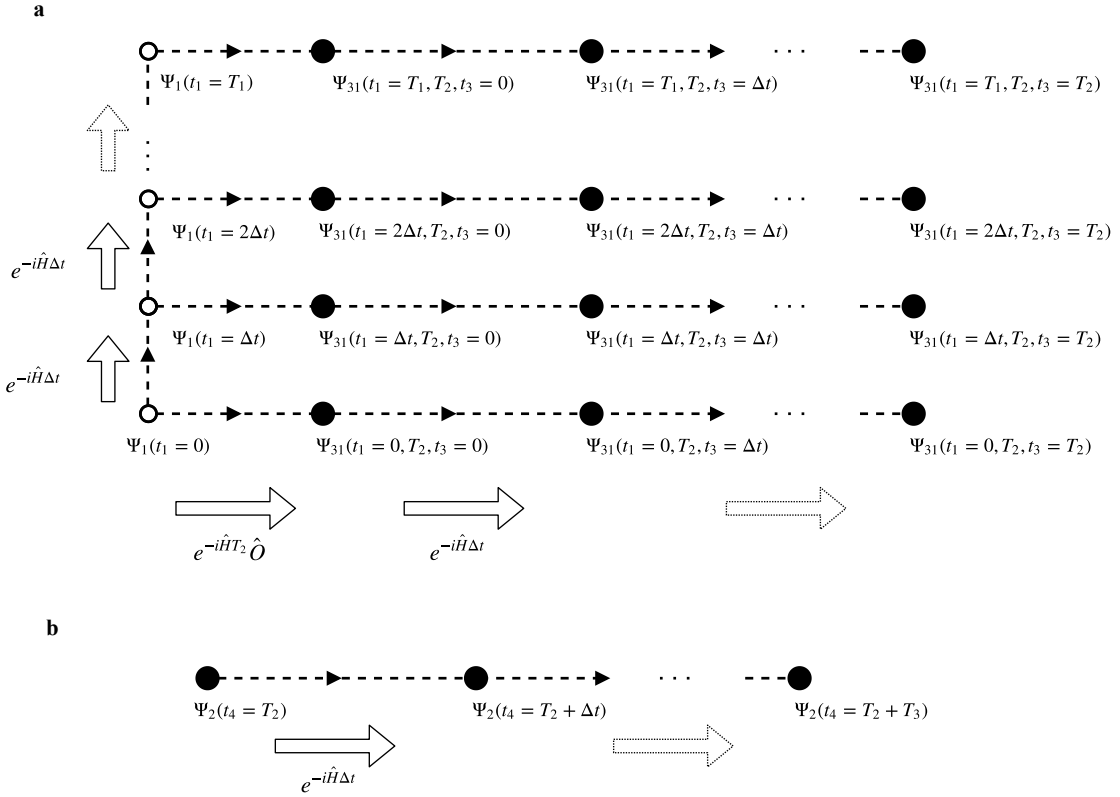


Figure 5.1: A schematic of the program used to sample $\langle \psi_{431} | \psi_2 \rangle$ as a function of t_1 and t_3 for the case of no dissipation.

Circles correspond to wavepackets, with those in **a** representing third order $|\psi_{431}\rangle$ and those in **b** corresponding to first order $|\psi_2\rangle$

t_1 takes values $0, \Delta t, 2\Delta t, \dots, T_1$ and similarly for t_3
 t_2 is fixed at T_2 for each spectra

Arrows pointing to the right and connecting an open and closed circle represent taking a copy of the wavepacket and evolving in t_2 for time T_2 .

Arrows pointing to the right and connecting two closed circles represent evolving the wavepacket and evolving in t_3 for Δt .

Arrows pointing up represent evolution in t_1 for Δt .

the value of $\langle \psi_{431} | \psi_2 \rangle$ separately for each of the combinations of t_1 and t_3 , is intractable even with the efficient simulation of dynamics described above. Specifically, if we have n time co-ordinates, each separated by Δt , in both t_1 and t_3 , and a value of t_2 equal to some multiple of this time gap, $m\Delta t$, then the total number of steps we need to compute is given by

$$\frac{3}{2}n^2(n+1) + 2n^2m \quad (\text{i.e } \mathcal{O}(n^3)) , \quad (5.11)$$

where each step corresponds to a propagation of a first- or third-order wavepacket for a time Δt .

Given that there are n^2 distinct co-ordinates for a fixed waiting time, we can at best use an algorithm of complexity $\mathcal{O}(n^2)$. I have therefore developed the following scheme, represented also in [Figure 5.1](#), that fulfils this condition for the case where $\gamma = 0$ (no dissipation):

1. Starting from the ground state, we apply the dipole operator to obtain $|\psi_1(t_1 = 0)\rangle$.
2. A copy of this state, $|\psi_1\rangle'$, can be evolved for all m steps in t_2 , giving $|\psi_1(t_1 = 0, t_2)\rangle'$.
3. A second copy state, $|\psi_2(t_2 = 0)\rangle$ is also produced by exciting the ground state. This too is propagated for m time steps to give $|\psi_2(t_2, t_3 = 0)\rangle$.
4. Applying the de-excitation operator to $|\psi_1(t_1 = 0, t_2)\rangle'$ gives $|\psi_{31}(t_1 = 0, t_2, t_3 = 0)\rangle$.
5. A copy of $|\psi_{31}(t_1 = 0, t_2, t_3 = 0)\rangle$ can be excited to give $|\psi_{431}(t_1 = 0, t_2, t_3 = 0)\rangle$.
6. The overlap $\langle \psi_{431} | \psi_2 \rangle$ ($t_1 = 0, t_2, t_3 = 0$) can now be calculated and stored.
7. Both $|\psi_{31}(t_1 = 0, t_2, t_3 = 0)\rangle$ and $|\psi_2(t_2, t_3 = 0)\rangle$ can be propagated for one step in t_3 , giving $|\psi_{31}(t_1 = 0, t_2, t_3 = \Delta t)\rangle$ and $|\psi_2(t_2, t_3 = \Delta t)\rangle$.
8. A copy of $|\psi_{31}(t_1 = 0, t_2, t_3 = \Delta t)\rangle$ can be excited to give $|\psi_{431}(t_1 = 0, t_2, t_3 = \Delta t)\rangle$.
9. The overlap $\langle \psi_{431} | \psi_2 \rangle$ ($t_1 = 0, t_2, t_3 = \Delta t$) can now be calculated and stored.
10. Steps 7-9 are repeated $n - 2$ more times, giving a $\langle \psi_{431} | \psi_2 \rangle$ ($t_1 = 0, t_2$) for all values of t_3 .
11. The original $|\psi_1(t_1 = 0)\rangle$ is evolved for Δt .
12. Steps 2-11 are repeated $n - 1$ more times, giving $\langle \psi_{431} | \psi_2 \rangle$ (t_2) for all values of t_1 and t_3 .

The total number of propagations is thus given by:

$$2n(n + m) + n = 2n^2 + 2nm + n . \quad (5.12)$$

This can be further improved by noting that the first order wavepacket does not depend on t_1 , and so a local version can be stored as a function of t_3 , requiring only $n + m$ steps. Also, all third-order wavepackets require being propagated in t_2 for m steps. This can be done at the very beginning, meaning that only m rather than $n * m$ propagations need be done.

With these optimisations, the number of propagations is:

$$n^2 + 2m + n \quad (5.13)$$

Although of the same order as [Equation 5.12](#), for large $m \sim n$, this can realise a $\sim 75\%$ increase in performance.

2D ECS is not a single molecule spectroscopy. As such, in order to simulate a real-life spectrum, we must average over many conformations of the polymer. This corresponds to running the simulation for different Hamiltonians, and so computation time is linear with respect to the number of contributing conformations.

5.3.2 Open System Case

In order to provide realistic results for the case of an open system, many quantum jump trajectories need to be averaged over. Experimentally, the time signal $\langle \psi_{431} | \psi_2 \rangle$ is collected separately for each unique value of (t_1, t_2, t_3) . This corresponds to each point in the total time signal having a unique set of quantum jump trajectories. As mentioned previously, it is not feasible to calculate $\langle \psi_{431} | \psi_2 \rangle$ separately for each data point - even with the optimised procedure for the isolated case, a contribution to the spectrum from a single conformation for a single t_2 time can still take up to 50 CPU days to be obtained.

We therefore modify the algorithm for the isolated case to provide as many quantum jump trajectories as possible in the time signal while still keeping the $\mathcal{O}(n^2)$ complexity:

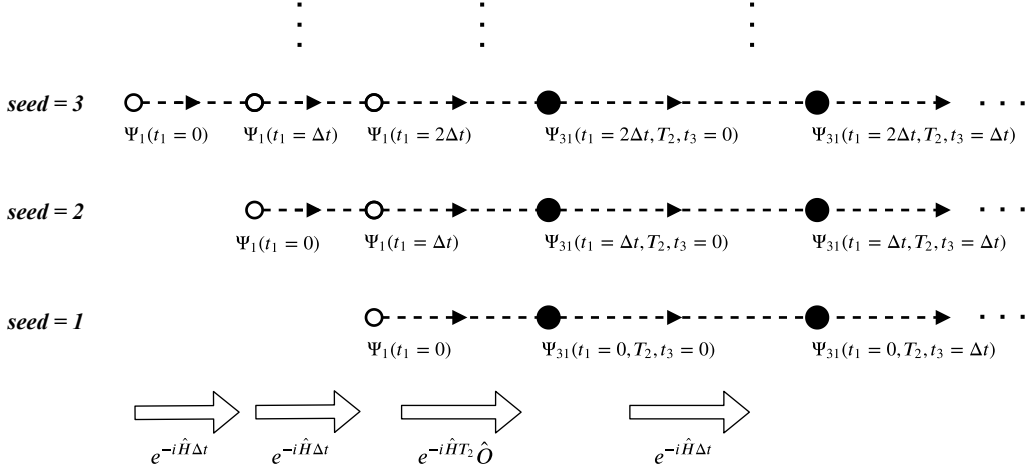


Figure 5.2: A schematic of the program used to sample $\langle \psi_{431} | \psi_2 \rangle$ as a function of t_1 and t_3 for the case with dissipation. The same representation scheme is used, and the same algorithm is applied to the first order wavepacket as in **b** of Figure 5.1. Additionally, arrows pointing to the right and connecting two open circles represent evolution in t_1 for a time Δt

- For each value of t_1 , steps 2-10 are performed. This corresponds to a single quantum jump trajectory.
 - Instead of propagating the initial $|\psi_1(t_1 = a\Delta t)\rangle$ for a single time step, a new $|\psi_1(t_1)\rangle$ is excited from the ground state and propagated for $(a + 1)$ time steps before steps 2-10 are repeated. This corresponds to a unique quantum jump trajectory for each value of t_1 .

The total number of steps is therefore given by

$$\frac{5}{2}n^2 + 2mn + \frac{n}{2} . \quad (5.14)$$

Repeating this procedure l times gives $l \times n$ contributing quantum jump trajectories to a single spectrum.

For a single calculation, the time signal does not show the same behaviour in t_1 and t_3 . This is shown in Figure 5.3. The use of this procedure can be justified, however, by noting that upon summing over many of these calculations, the time signal becomes smooth in both dimensions, as is seen in Figure 5.4.

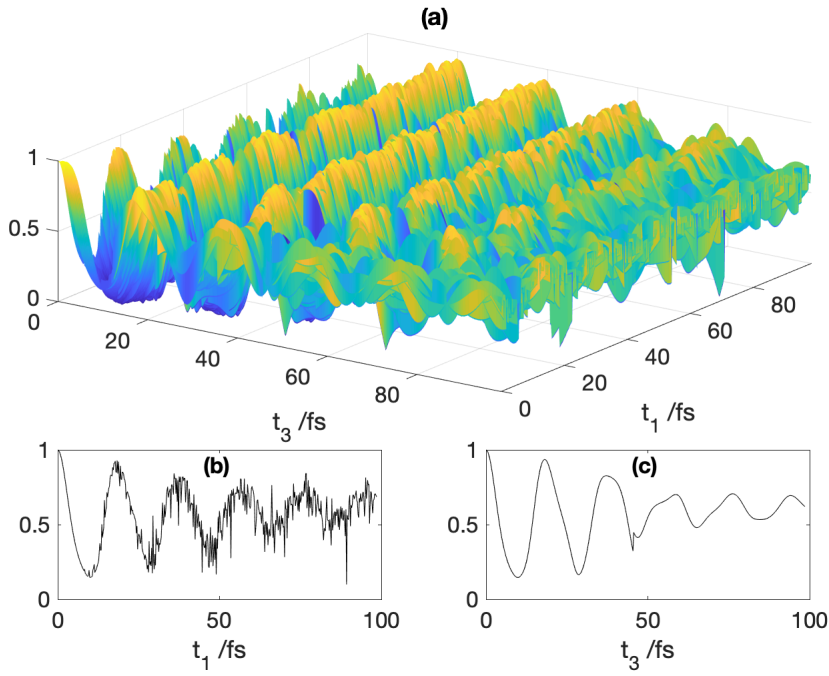


Figure 5.3: three plots showing $|\langle \psi_{431} | \psi_2 \rangle|$, as produced from a single calculation with $\gamma = 0.2\hbar\omega$. (a) is plotted against both t_1 and t_3 . (b) shows $|\langle \psi_{431} | \psi_2 \rangle(t_3 = 0)|$. (c) shows $|\langle \psi_{431} | \psi_2 \rangle(t_1 = 0)|$. The plots are smooth for a fixed value of t_1 , but rough for fixed t_3

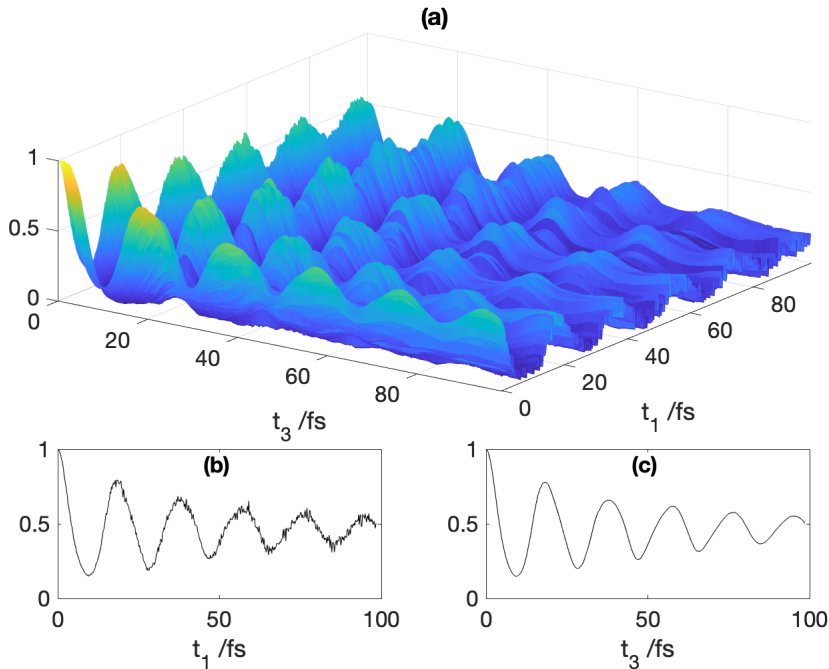


Figure 5.4: the same plots as shown in Figure 5.3, as averaged over multiple calculations. The smoothness in t_1 is now similar to that in t_3 .

Chapter 6

The Discrete Fourier Transform and Signal Processing

The previous chapters have outlined the theory and procedures necessary for us to simulate the dynamics of the system and obtain the discrete time signal of interest. Transforming this into an accurate spectrum is not straightforward. In this chapter, we therefore introduce the discrete Fourier transform (DFT), and the steps required to produce a spectrum.

6.1 The Discrete Fourier Transform

The one-dimensional DFT is a discrete approximation of the continuous one-dimensional Fourier transform. Thus, it converts a discrete and finite time signal into a discrete and complex valued frequency spectrum^{52 53}

$$F(\omega) = \sum_{n=0}^{N-1} f(t_n) e^{-i\frac{2\pi}{N}n\omega}. \quad (6.1)$$

The time signal must be sampled at equal spacings in time $\{t_n\}$, given by

$$t_n = t_0 + n\Delta t, \quad (6.2)$$

with a total length of $(N - 1)\Delta t = T$. This leads to sampling of the DFT at frequencies $\{\omega_m\}$ given by

$$\frac{\omega_m}{2\pi} = \frac{m}{T} - \frac{1}{2\Delta t}, \quad (6.3)$$

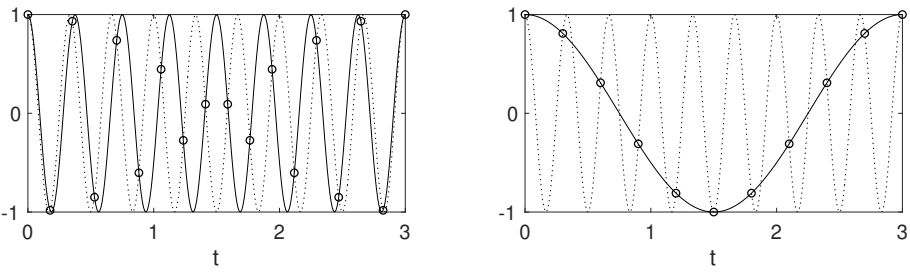


Figure 6.1: Undersampling.

A continuous time signal (dashed line) being sampled (circles) at two different frequencies, both above the Nyquist limit, leading to a discrete time signal suggesting an original signal of lower frequency (solid line).

This is manifested as reflection back into the DFT frequency range, giving spurious peaks.

where both $n, m \in 0, 1..N - 1$ such that N samplings of the time signal gives N samplings of the frequency spectrum.

Generalising to two- and higher-dimensional Fourier transforms is trivial; one need only apply successive 1D DFTs with respect to each of the time dimensions.

6.1.1 Undersampling

As can be seen from [Equation 6.3](#), the maximum (Nyquist) frequency detectable is $1/2\Delta t$. Thus, for a time signal containing a maximum frequency component of ω_{max} , the time period between samplings can at most be^{[53](#),[54](#)}

$$\Delta t_{max} = \frac{2\pi}{\omega_{max}} \quad (6.4)$$

in order to accurately detect this frequency. If a larger time period of sampling is used, undersampling occurs, whereby the frequency of oscillation is reflected back into the DFT, giving spurious peaks. A visualisation of how this occurs is given in [Figure 6.1](#).

Throughout this work, care has been taken to ensure that the Nyquist frequency lies well above the highest frequency component expected in the spectrum.

6.1.2 Peak Separation

It can also be seen from [Equation 6.3](#) that the spacing between samplings of the DFT is given by $1/T$. Thus, perhaps counterintuitively, to get a closer approximation of the true Fourier transform (by sampling more closely in the frequency domain), one needs to

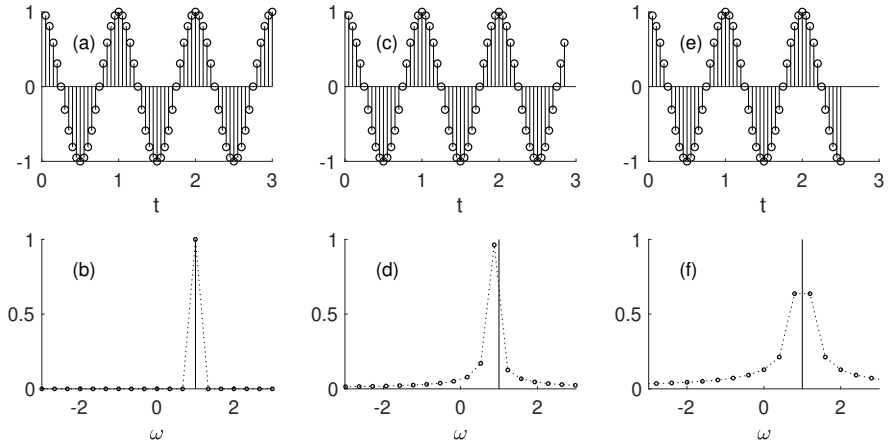


Figure 6.2: Spectral Leakage.

(a), (c) and (e) show the real part of the time signal $e^{-i2\pi t}$ for $t = 0$ to 3 , 2.7 and 2.5 respectively.

(b), (d) and (f) are the absolute values of the DFT for the respective time signal.

Time signal (a) is sampled over an integer number of time periods. Thus (b) shows a δ -peak, centred at $\omega = 1$.

Time signal (b) is sampled over a non-integer number of time periods. Thus (d) shows spectral leakage, and is far from a δ -peak. The maximum is shifted away from $\omega = 1$.

These effects are maximally pronounced in (c) and (f).

sample the time signal for a longer overall time rather than at closer intervals.

Specifically, in order to separate two δ -peaks $\Delta\omega$ apart, one needs to sample the signal for a total time $T \geq 4\pi/\Delta\omega$. This sampling time needs to be longer for non δ -function peaks, in order to resolve the lineshape of each peak separately.

6.1.3 Spectral Leakage

A further condition to obtain a perfectly accurate spectrum is that the time signal is taken over an integer number of time periods.^{53,54} When this is the case, for the example of a time signal with a single frequency component, $f(t) = e^{i2\pi\omega_0 t}$, the DFT gives a discrete delta function: $F(\omega) = \delta(\omega, -\omega_0)$.

As can be seen in Figure 6.2, when the signal is not sampled over an integer number of time periods, spectral leakage occurs. This gives rise to three undesirable features in the spectrum simultaneously:

- **intensity reduction:** the intensity of the peak is reduced such that it is no longer equivalent to the coefficient of the term oscillating at frequency ω_0 .
- **lineshape broadening:** the lineshape is no longer a discrete sampling of a δ -peak.

The peak is broadened, indicative of a decay in the time signal which is not actually present.

- **frequency shift:** the frequency of the maximum in the peak is shifted, giving an incorrect measurement of ω_0 .

These features are most pronounced when the time signal is sampled over a half odd integer number of time periods, but are still evident for long times and small deviations from the ideal integer number time periods.

For a time signal containing a single oscillating component, it is trivial to choose a sampling time period and length of signal such that no spectral leakage occurs. For a signal composed of many oscillating components, it is not in general possible to eliminate spectral leakage completely.

In this work, we have taken the approach of taking N data points separated by constant Δt to sample in both t_1 and t_3 . We then produce spectra from time signals for various values of $N_1, N_3 \leq N$, corresponding to the length of the time signal used in t_1 and t_3 respectively, and select the spectrum with the lowest amount of spectral leakage. To measure the spectral leakage of a spectrum, we use the entity

$$G(N_1, N_3) = \frac{1}{N_1 N_3} \left[\sum_{\omega_1, \omega_3} F_{(N_1, N_3)}(\omega_1, \omega_3) - \sum_{\text{peaks}} F_{(N_1, N_3)}(\omega_1, \omega_3) \right], \quad (6.5)$$

which corresponds to the average height of the DFT at frequencies not corresponding to local maxima (peaks), and hence we choose N_1 and N_3 that minimise this function.

6.2 Signal Processing

In this work, preparing an accurate spectrum is therefore difficult:

1. The computation time, as detailed in [Chapter 5](#), is $\propto N^2$. Hence the number of samples we take is to be minimised in order to ensure reasonable calculation times.
2. The signal must be sampled over ~ 100 fs in both t_1 and t_3 in order to provide good separation between peaks spaced 0.2 eV apart.
3. The spacing in time between successive data points must be less than ~ 0.5 fs in order to avoid undersampling. The smaller Δt is, the more values of N_1 and N_3 we

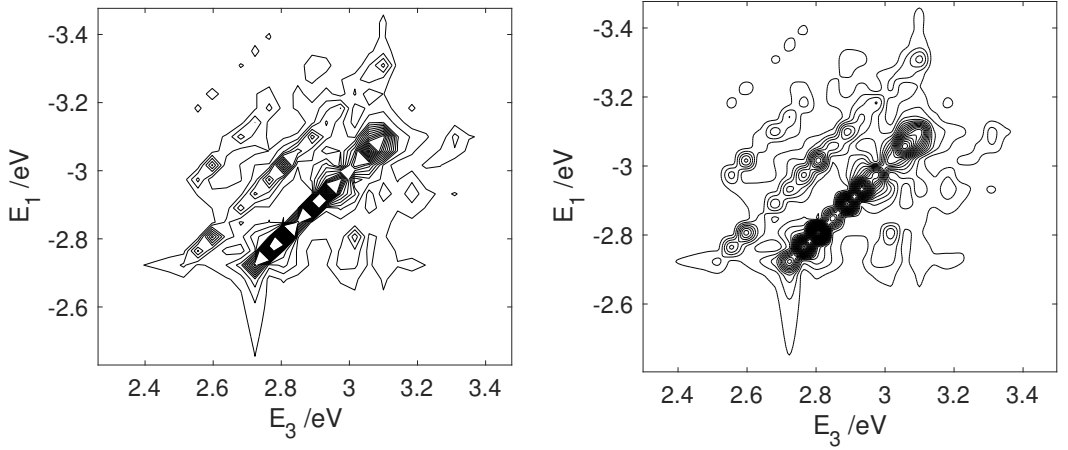


Figure 6.3: The left plot shows a spectrum before smoothing. Peak positions are not necessarily obvious, with strange square and triangular artefacts arising from poor frequency resolution over which to take a contour.

The right plot shows the spectrum with contours taken over an interpolated surface. Peak positions are much clearer, and the spectrum is much more easily interpreted without any introduction of spurious information.

can try, leading to a spectrum with less spectral leakage, but the longer the computation takes. We have therefore used a value of $\Delta t = 0.25 \text{ fs}$, having found that this gives accurate spectra while placing an upper limit on the computation time for a complete time signal calculation at 100 CPU days.

6.2.1 Spectrum Representation

As mentioned in [Chapter 4](#), we plot as a spectrum the absolute value of the Fourier transform of $\langle \psi_{431} | \psi_2 \rangle$ with respect to t_1 and t_3 . We represent the resulting function of E_1 and E_3 using a contour plot, where closed lines correspond to points with equal intensity. The relatively poor resolution in E_1 and E_3 results in square and triangular line shapes when the raw signal is contoured, which act to obscure peak shapes and features of interest in the spectra. We therefore employ a cubic interpolation scheme on the absolute value of the frequency signal. This passes through all original points in the frequency signal, with the sole effect of rounding the contours such that the interpretation of a spectrum becomes much easier, as shown in [Figure 6.3](#).

Chapter 7

Results and Discussion

The main results obtained in this work are presented in this chapter. We first derive the analytical solution for the case of an isolated monomer. This is instructive when considering the vibrational structure of all spectra produced in this work.

The spectrum for an isolated 20 monomer chain is then related to the single monomer case. The analysis of this provides insights into the ultrafast dynamics detailed in [Chapter 3](#) which are dependent solely on the Frenkel-Holstein parameters. The effects of inhomogeneous broadening on the spectrum are also analysed.

The spectra for the above two chain lengths are also presented with dissipation included in the dynamics. These spectra are analysed with respect to those for the isolated systems to isolate the effects of dissipation.

7.1 Isolated Systems

7.1.1 Single Monomer

We can start to derive the analytical form of the overlap $\langle \psi_{431} | \psi_2 \rangle$ for the single monomer case by noting that the Frenkel-Holstein Hamiltonian reduces to

$$\begin{aligned}\frac{\hat{H}}{\hbar\omega} &= \frac{E_0}{\hbar\omega} \hat{N} - A \hat{N} \frac{(b^\dagger + b)}{\sqrt{2}} + b^\dagger b , \\ &= \tilde{E}_0 \hat{N} - \lambda \hat{N} (b^\dagger + b) + b^\dagger b .\end{aligned}\tag{7.1}$$

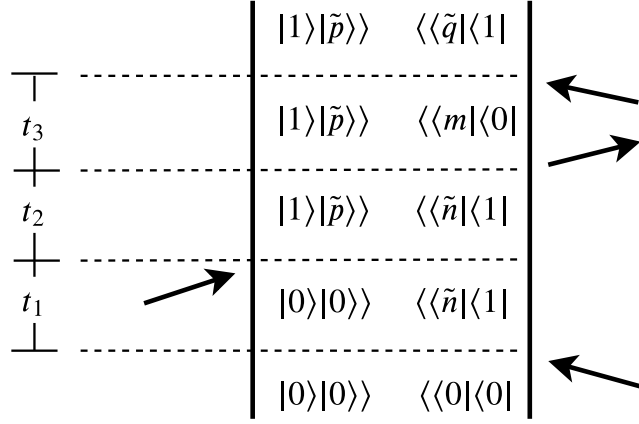


Figure 7.1: Double-sided Feynman diagram representing $\langle \psi_{431} | \psi_2 \rangle$ for the isolated monomer case

Using the Lang-Firsov transformation,⁵³ $b = \tilde{b} + \lambda$, gives

$$\begin{aligned}\frac{\hat{H}_{GSM}}{\hbar\omega} &= \hat{H}'_{GSM} = b^\dagger b ; \\ \frac{\hat{H}_{ESM}}{\hbar\omega} &= \hat{H}'_{ESM} = \tilde{E}_0 + \tilde{b}^\dagger \tilde{b} - \lambda^2 ,\end{aligned}\quad (7.2)$$

where GSM and ESM stand for the ground and excited state manifold respectively, and \tilde{b} is the displaced vibrational lowering operator. The eigenstates of \hat{H}'_{GSM} are $\{|0\rangle|n\rangle\}$, where $|n\rangle$ are the SHO eigenstates, with energies $\tilde{E}_n = n$. The eigenstates of \hat{H}'_{ESM} are $\{|1\rangle|\tilde{m}\rangle\}$, where $|\tilde{m}\rangle$ are the displaced SHO eigenstates, with energies $\tilde{E}_m = m + \tilde{E}_0 - \lambda^2 = m + \tilde{E}'_0$. We can relate the two sets of eigenstates

$$\begin{aligned}|\tilde{m}\rangle &= \frac{(\tilde{b}^\dagger)^n}{\sqrt{m!}} |0\rangle \\ |n\rangle &= \frac{(\hat{b}^\dagger)^n}{\sqrt{n!}} |0\rangle\end{aligned}\quad (7.3)$$

using

$$|\tilde{0}\rangle = e^{-\frac{\lambda^2}{2}} \sum_q \frac{\lambda^q}{\sqrt{q!}} |q\rangle . \quad (7.4)$$

It is useful to write $V_{n,m} = \langle \langle \tilde{n} | m \rangle \rangle = \langle \langle m | \tilde{n} \rangle \rangle$. This can be evaluated exactly for $m \geq n$

as

$$V_{n,m} = e^{-\frac{\lambda^2}{2}} \sqrt{\frac{m!}{n!}} \sum_{k=0}^n (-1)^k \lambda^{2k} \lambda^{(m-n)} \frac{{}^n C_k}{(k+m-n)!}, \quad (7.5)$$

with $V_{n,m} = (-1)^{m+n} \cdot V_{m,n}$. At $t = 0$, the ground state is given by: $|GS\rangle = |0\rangle|0\rangle$.

Applying a vertical excitation leaves the oscillator in the same vibrational state

$$|EX\rangle = \hat{a}_n^\dagger |GS\rangle = |1\rangle|0\rangle, \quad (7.6)$$

where $|0\rangle$ can be written as a linear combination of $\{|\tilde{n}\rangle\}$

$$|0\rangle = \sum_n V_{n,0} |\tilde{n}\rangle. \quad (7.7)$$

Thus,

$$|\psi_1(t = t_1 + t_2)\rangle = |1\rangle \sum_{n=0} V_{n,0} \cdot e^{-i(\tilde{E}'_0 + n)(t_1 + t_2)} |\tilde{n}\rangle. \quad (7.8)$$

Vertical de-excitation at $t = t_1 + t_2$ gives

$$\begin{aligned} |\psi_{31}(t = t_1 + t_2)\rangle &= |0\rangle \sum_{n=0} V_{n,0} \cdot e^{-i(\tilde{E}'_0 + n)(t_1 + t_2)} |\tilde{n}\rangle \\ &= |0\rangle \sum_{n,m=0} V_{n,0} V_{n,m} \cdot e^{-i(\tilde{E}'_0 + n)(t_1 + t_2)} |m\rangle. \end{aligned} \quad (7.9)$$

Propagation in t_3 followed by a final vertical excitation gives

$$|\psi_{431}(t = t_1 + t_2 + t_3)\rangle = |1\rangle \sum_{n,m,p=0} V_{n,0} V_{n,m} V_{p,m} \cdot e^{-i(\tilde{E}'_0 + n)(t_1 + t_2) - imt_3} |\tilde{p}\rangle, \quad (7.10)$$

such that

$$\langle \psi_{431} | \psi_2 \rangle = \sum_{p,m,n=0} V_{n,0} V_{n,m} V_{p,m} V_{p,0} \cdot e^{i(\tilde{E}'_0 + n)t_1} \cdot e^{i(n-p)t_2} \cdot e^{-i(\tilde{E}'_0 + p - n)t_3}, \quad (7.11)$$

giving a spectrum of the form

$$\hat{\mathcal{F}}(\omega_1, t_2, \omega_3) = \sum C_{n,m,p} \cdot \delta(\omega_1 + \tilde{E}'_0 + n) \cdot \delta(\omega_3 - \tilde{E}'_0 - p + m) \cdot e^{i(n-p)t_2}. \quad (7.12)$$

The complex coefficients $C_{n,m,p}$ depend solely on the Frenkel-Holstein parameter A (or equivalently λ). For a small value of A , the only states with significant Franck-Condon overlaps with the ground vibrational state $|0\rangle$ are $|\tilde{0}\rangle$ and $|\tilde{1}\rangle$. This effectively reduces

	\tilde{n}	m	\tilde{p}		\tilde{n}	m	\tilde{p}
(1)	0	0	0	(5)	1	0	0
(2)	0	0	1	(6)	1	0	1
(3)	0	1	0	(7)	1	1	0
(4)	0	1	1	(8)	1	1	1

Table 7.1: possible pathways in the vibrational basis.
The labels 1 to 8 have been shown in Figure 7.2

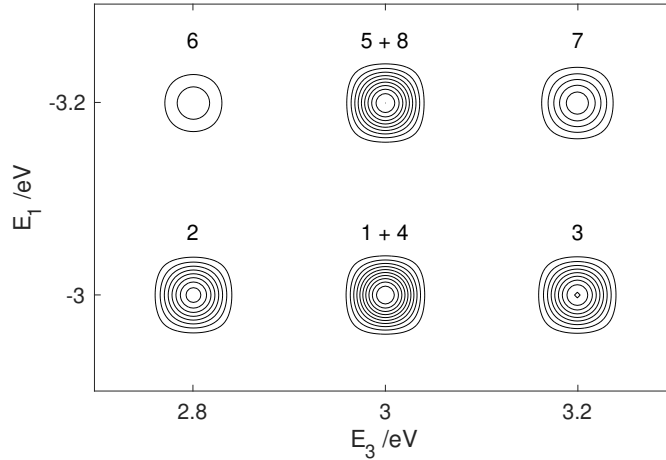


Figure 7.2: Spectrum for a single monomer chain with $t_2 = 0$: no dynamics are observed here. Physically realistic parameter values have been used: $A = 2$, $E'_0 = 3 \text{ eV}$ and $\hbar\omega = 0.2 \text{ eV}$.

the system to having two levels in the vibrational basis, as is physically realistic for conjugated polymers, and means that there are thus eight possible wavepacket pathways for the overlap $\langle \psi_{431} | \psi_2 \rangle$, shown in the double-sided Feynman diagram in Figure 7.1 and labelled in Table 7.1.

This leads to the observation of 6 peaks in the 2D ECS spectrum (Figure 7.2). Pathways 1, 3, 6 and 8 give contributions that are static in t_2 , while all others display Rabi-oscillations⁵⁶ in t_2 , meaning that the separation of the overlapping contributions 1 + 4 and 5 + 8 can be accomplished by plotting the spectrum for several values of t_2 . Alternatively, sampling frequently in t_2 allows a further dimension to be added to the spectrum, producing the 3D spectrum shown in Figure 7.3.

All peaks here are δ -functions. The isolated nature of the monomer means that there is no decay in the time signal, in turn meaning that there is no broadening of the line shapes.

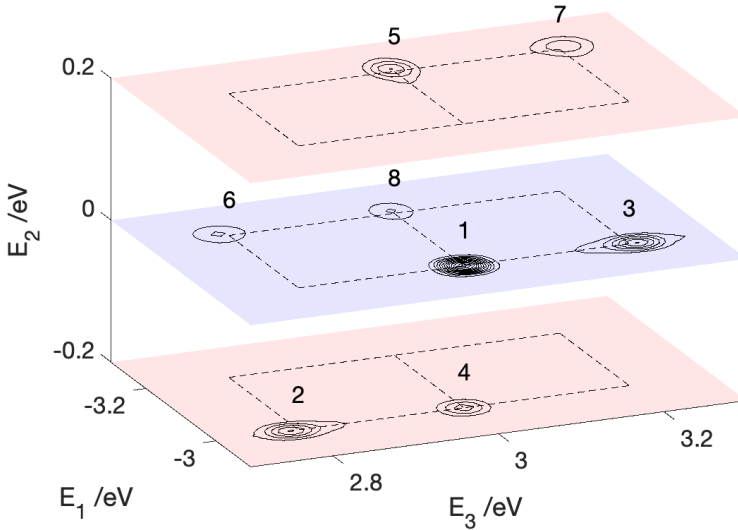


Figure 7.3: A 3D spectrum, showing separation of all peaks by transforming with respect to all three time dimensions.

7.1.2 Polymers

A disordered PPV polymer chain of 20 monomers, excited into two eigenstates of the Frenkel Hamiltonian, produces the spectrum in Figure 7.4. The vibrational structure of the four groups of peaks is identical to that seen for the single monomer case, allowing for the fact that the same coupling parameter A gives lower Franck-Condon overlaps for non 0–0 transitions in larger chains. The diagonal peaks correspond to evolution in either $j = 1$ or $j = 4$ for both t_1 and t_3 , while the off-diagonals correspond to evolution in $j = 1$ for t_1 and $j = 4$ for t_3 , and vice versa, where j is the exciton COM quantum number.

Figure 7.4 is the spectrum with minimal spectral leakage. The increased number of frequency components here relative to the single monomer case means that we see an increase in spectral leakage in any one spectrum, however, and this manifests itself in the form of spurious linewidths and different intensities for what are identically populated states. Analysing the spectra for several different values of N_1 and N_3 , as in Chapter 6, shows, however, that all peaks are in fact δ -functions, and moreover that all the vibrational structures are identical, with equal intensities for the corresponding peaks in all four quadrants, something which unfortunately cannot be shown on a single spectrum. (The peaks

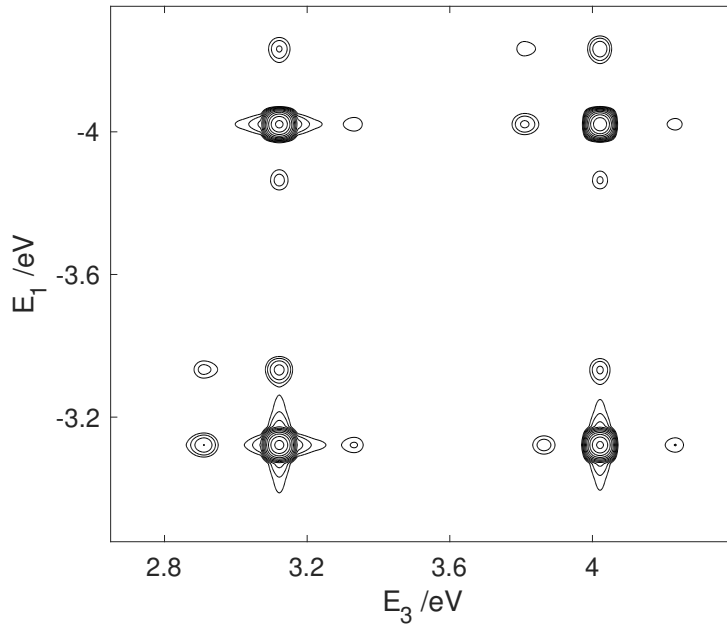


Figure 7.4: Spectrum of a 20 site disordered chain excited into the 1st LEGS ($j = 1$) and 1st QEES ($j = 4$) for $t_2 = 0\text{fs}$. No dynamics are observed in this spectrum. The parameters used are given in [Table 2.1](#).

in this particular spectrum at $\sim 3.85 \text{ eV}$ in E_1 are labelled as artefacts of the DFT: they are not observed for other values of N_1 and N_3 , and their separation from the 0–0 peaks is unphysical, not being equal to a multiple of $\hbar\omega$.)

The fact that the spectrum is a sum of δ -functions means that we are not observing any relaxation dynamics here; more specifically, the amplitude of the contributions to the overlap $\langle \psi_{431} | \psi_2 \rangle$ oscillating at specific E_1 and E_3 remain constant during all of t_1 and t_3 for a fixed t_2 . As a function of t_2 , we see undamped Rabi oscillations of the peaks in the spectrum, with time periods corresponding to units of $\hbar\omega$ for the diagonal peaks, with an additional contribution from the difference in energy between the LEGS and QEES for the off-diagonal peaks.

Disorder Average

The above spectrum has been taken from a single instance of disorder, replicating a single-molecule spectroscopy. Experimentally, however, spectra are produced from signals that average over many polymer chains, and therefore conformations, simultaneously. We can thus simulate the expected experimental spectra by summing the time signal from

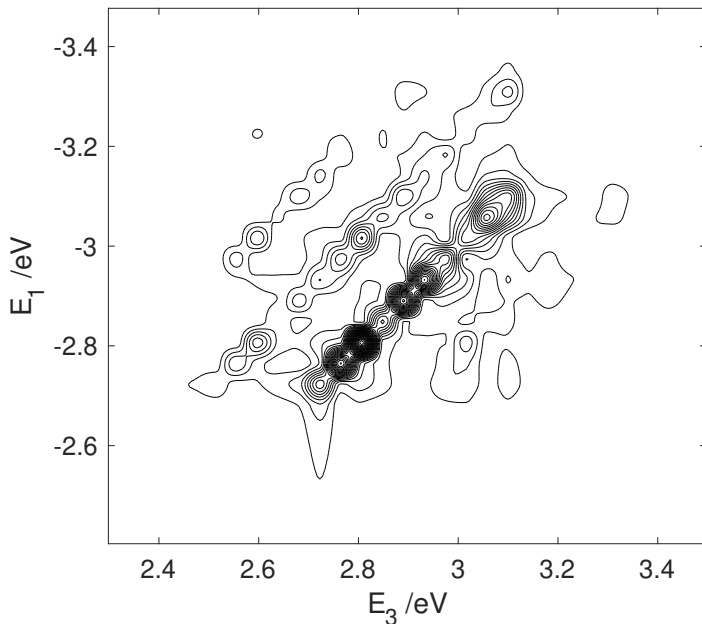


Figure 7.5: Inhomogenous broadening seen for a single LEGS.

many different polymer conformations before taking a spectrum. The effect this has on the spectrum is best illustrated by exciting solely into the $j = 1$ LEGS, as shown in Figure 7.5.

The linewidth here is not indicative of relaxation dynamics: a perfect Fourier transform would reveal an array of δ -functions corresponding to the discrete energies of the eigenstates for different polymer conformations. In practice, the time signal can not be measured for long enough to resolve each peak separately. Combined with unavoidable spectral leakage, this gives rise to a noisy spectrum. The primary, elongated peak corresponds primarily to the dominant 0–0 and the 0–1 transition pathways (labelled ① and ④ in Table 7.1), with its diagonal, or inhomogeneous, linewidth reflecting the distribution of energies of the lowest LEGS as a function of disorder.

7.2 Open Systems

7.2.1 Single Monomer Case

No simple analytical solution exists for the single monomer case when dissipation is included. The spectrum obtained from many quantum jump trajectory simulations (Chapter 5) for the single monomer case allows analysis of the vibrational relaxation that dis-

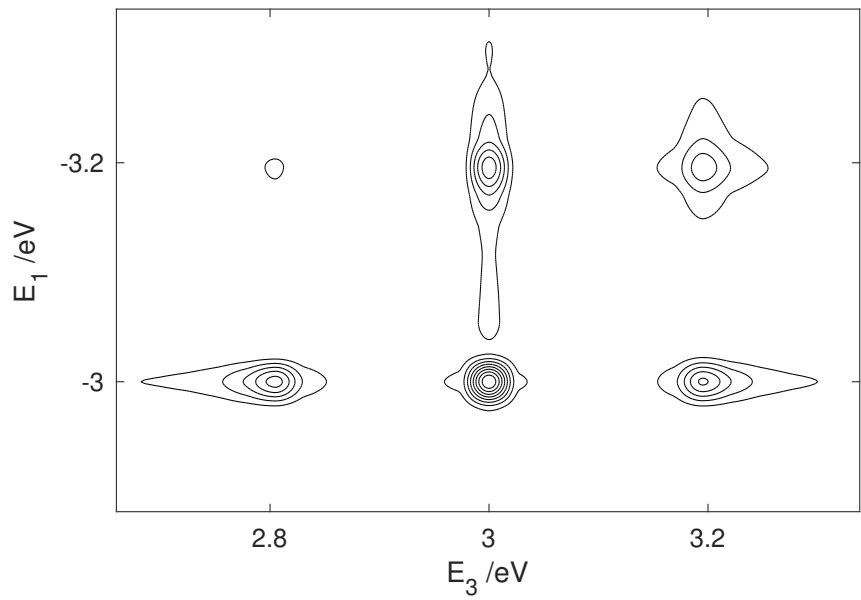


Figure 7.6: Spectrum of a single monomer, with $\gamma = 0.2\hbar\omega$.
 $t_1, t_3 = 0 \rightarrow 100 \text{ fs}$. $t_2 = 5 \text{ fs}$.

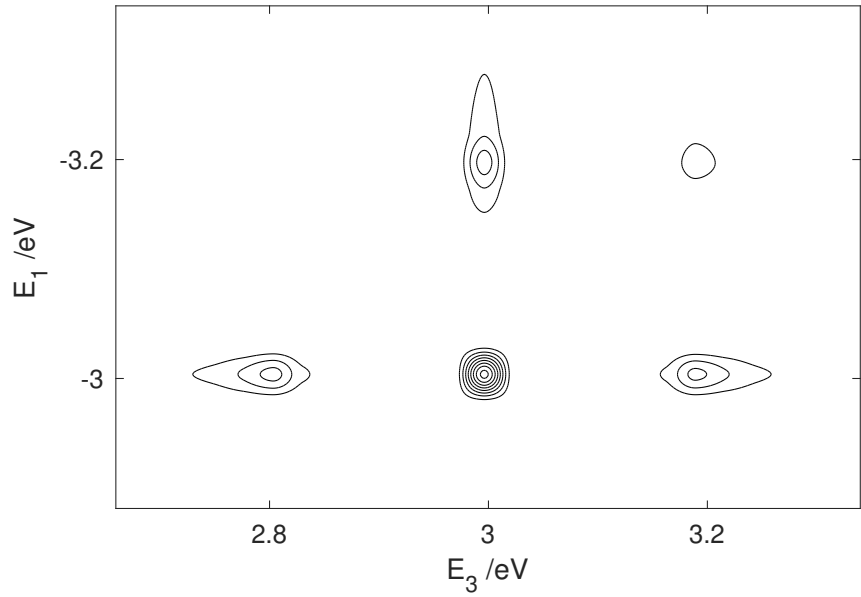


Figure 7.7: Spectrum of a single monomer, $\gamma = 0.2\hbar\omega$.
 $t_1, t_3 = 0 \rightarrow 100 \text{ fs}$. $t_2 = 35 \text{ fs}$.

sipation induces, without the complication of exciton dynamics. Several features in both [Figure 7.6](#) and [Figure 7.7](#) indicate this vibrational relaxation:

- **lineshape:** peaks are a convolution of δ -function and Lorentzian lineshapes. A peak corresponding to evolution in the vibrational ground state in t_1 will have a δ -function line shape in E_1 , while a peak corresponding to evolution in the excited state in t_1 will have a Lorentzian line shape in E_1 (and similarly for t_3 and E_3). Thus the lineshape of the 0–0 contribution, labelled ① in [Table 7.1](#), remains unchanged relative to the isolated case. The 1–1 peak, labelled ⑦, shows line broadening in both E_1 and E_3 .
- **amplitude:** for an isolated monomer, the amplitude of excited peaks are comparable to the 0–0 peak, as seen in [Figure 7.2](#). The amplitude of the non 0–0 peaks when dissipation is included, however, are greatly reduced, more so than can be purely justified by noting their increased width. We can understand this by noting that the spectrum can be viewed as the amplitude of components oscillating at certain frequencies, as averaged over all the data points in the input time signal. At long times, the system is predominantly found only in the vibrational groundstate, meaning that we therefore observe much lower amplitudes for all peaks corresponding to excited states.
- **dynamics in t_2 :** comparing the spectrum for $t_2 = 5$ fs against that for $t_2 = 35$ fs shows that significant relaxation occurs in the first 35 fs: there is only a very small population left in the vibrationally excited state, as evidenced by the decrease in amplitude of peaks ②, ③ and ⑦ in [Figure 7.7](#). The half-life of the decay is constant however, and so the half-height width of these peaks is independent of t_2 .

7.2.2 Polymers

LEGS

As has been observed by *Mannouch et al.*,⁹ the dynamics of LEGS are less pronounced than for QEES: the exciton COM wavefunction is given by the lowest energy eigenstate of the Frenkel Hamiltonian, such that we only observe vibrational relaxation, with the very small further exciton localisations that these bring. Thus, the spectrum for a 20 monomer

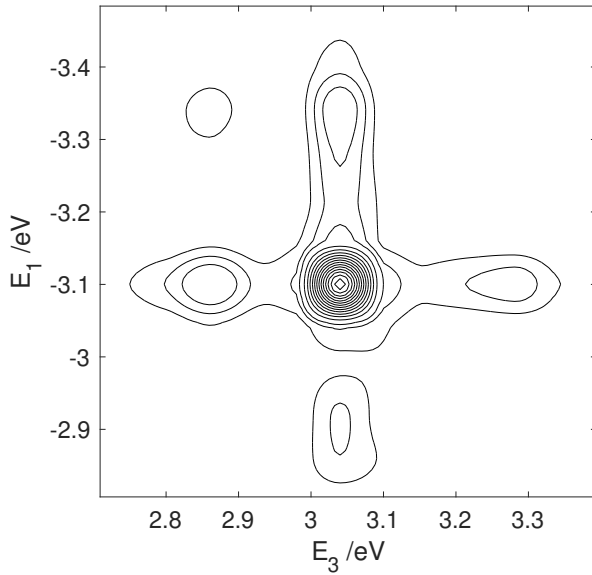


Figure 7.8: Spectrum of a 20 monomer PPV chain, excited into the $j = 1$ LEGS. $t_1, t_3 = 0 \rightarrow 100\text{fs}$. $t_2 = 0\text{fs}$. Vibrational relaxation leads to directional broadening of vibrationally excited peaks.

PPV chain, given in Figure 7.8, is qualitatively very similar to that for the single monomer case. The main difference is, as previously mentioned, the further reduced intensities of the vibrationally excited peaks due to weaker Franck-Condon overlaps for extended chains.

QEES

All peaks in Figure 7.9 show broadening in both E_1 and E_3 , corresponding to the relaxation of, and population loss from, the QEES. Where vibrational relaxation is also taking place, this broadening is enhanced. The amplitude of the QEES peak is significantly lower than for the LEGS peak, as can be seen in Figure 7.10, where the system is initially excited into a 1:1 linear combination of a LEGS and QEES, and this acts as a further indicator of the population loss, as explained above.

In their work, *Mannouch et al.*⁴ were able to identify which LEGS the QEES relax onto (see Figure 3.3), but evidently this is not the case here. The incoherent nature of the localisation means that we do not see any peaks corresponding to the LEGS: contributions from different quantum jump trajectories give different, random phases to the contributions to the signal produced by the LEGS. Averaging over many trajectories leads to destructive interference of these signals, and as such, no coherent time signal contribution from the

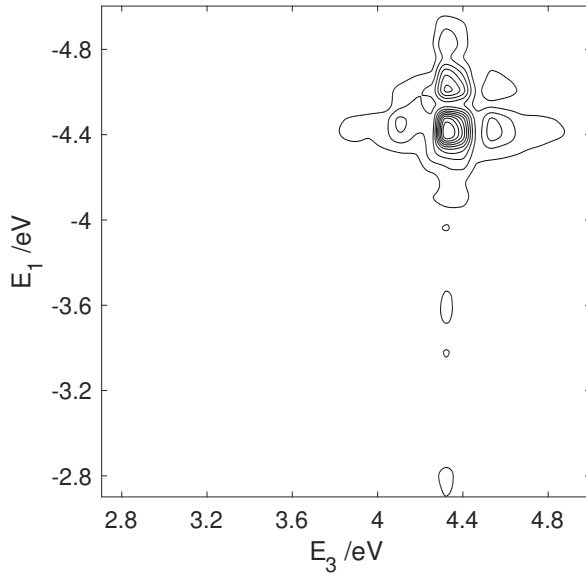


Figure 7.9: Spectrum of a 20 monomer PPV chain, excited into the $j = 4$ QEES.
 $t_1, t_3 = 0 \rightarrow 100\text{fs}$. $t_2 = 0\text{fs}$. Vibrational relaxation leads to directional broadening of vibrationally excited peaks. Further broadening is seen for all peaks due to population loss.

LEGS is seen.

Off-Diagonal Coherences

As mentioned in [Chapter 5](#), a typical polymer chain will only absorb strongly into a few eigenstates of the Frenkel Hamiltonian. We therefore also present a spectrum for a polymer chain excited into a 1:1 linear combination of the $j=1$ LEGS and $j=4$ QEES in [Figure 7.10](#).

The off diagonal peaks correspond to ground state mediated couplings between the LEGS and QEES and thus display differential broadening with respect to t_1 and t_3 : the upper left peak corresponds to contributions to system that are evolving in the QEES during t_1 and the LEGS during t_3 . As such, significant broadening is seen in the E_1 axis, while almost none is observed in the E_3 axis, and vice versa for the bottom right peak. The amplitudes of these peaks are determined by the geometrical mean of that for the LEGS and that for the QEES.

One quarter of the system undergoes the same pathway as that for excitation purely into a LEGS. The remaining three quarters undergo pathways which lead to relaxation onto the LEGS, but the incoherent nature of this relaxation means that no change to the

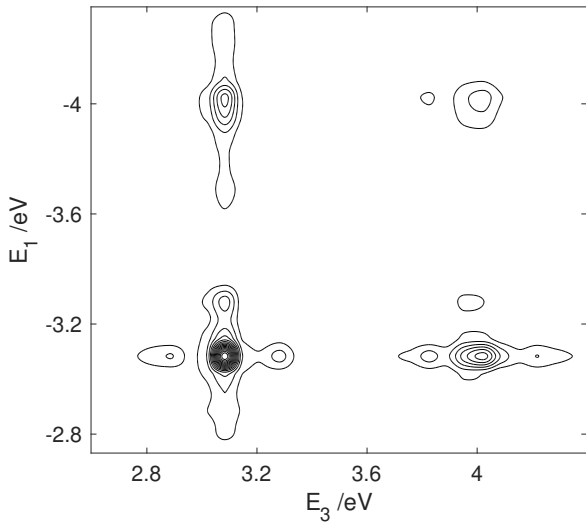


Figure 7.10: Spectrum of a 20 monomer PPV chain, excited into an equal contribution of the $j = 1$ LEGS and $j = 4$ QEES. $t_1, t_3 = 0 \rightarrow 100\text{fs}$. $t_2 = 0\text{fs}$. Weak amplitude of QEES peak corresponds to rapid population loss. Line-shape of coherences reflect this.

0–0 LEGS peak is seen relative to to Figure 7.8.

7.3 Discussion

The aim of this work was to ascertain the extent to which ultrafast excitonic dynamics could be identified and analysed in 2D ECS spectra, specifically the processes of exciton-polaron formation, exciton site decoherence and exciton-localisation.

The former two of these have been shown to occur irrespective of the presence of dissipation.⁴ We have not observed any manifestation of these using 2D ECS spectroscopy, however, in either the open or closed system cases.

We can rationalise this by first noting that the wavefunction of any excited state at the instant of excitation can be written as $|\psi_{ex}\rangle = \sum_a c_a |a\rangle$ where $\{|a\rangle\}$ are the eigenstates of H_{FH} , and, with no dissipation present in the system, this state will evolve according to $|\psi_{ex}(t)\rangle = \sum_a c_a e^{-iE_a t} |a\rangle$. In analogy to the single monomer case, the final overlap can therefore be written as:

$$\langle \psi_{431} | \psi_2 \rangle = \sum_{a,b,c} C_{a,b,c} \cdot e^{iE_a t_1} \cdot e^{i(E_a - E_b)t_2} \cdot e^{i(E_c - E_b)t_3} \quad (7.13)$$

where, importantly, $C_{a,b,c}$ is a constant due to a lack of dissipation.

This facilitates a better understanding of exciton-site decoherence: the initial state upon excitation is a linear combination of eigenstates, with all coefficients in phase. As time progresses, the complex coefficients of these rotate at the energies of the eigenstates. The distribution of energies of the different states, together with the fact that no one state is dominantly populated means that the coefficients of the eigenstates quickly dephase with respect to each other. In the polymer site basis, this gives rise to rapid randomisation of the phase of the exciton on each monomer, meaning that the exciton-site coherence length rapidly decays in time. Left for arbitrarily long time, the coefficients of the eigenstates will come partially and completely back into phase, such that the coherence length will grow back to its value for the initially excited state. Thus, this decoherence is only temporary, and is a manifestation of the rapid destructive interference of different frequency terms. In practice, complete constructive interference occurs after a time equal to the lowest common multiple of the time periods of all the contributing frequencies, and so is not seen in the first 100 fs of dynamics in [Figure 3.2](#) (partial constructive can be seen, however, at multiples of the time period of the SHO oscillations). The same argument applies to exciton-polaron formation: for long enough times $\gg 100$ fs, the correlation between the exciton COM and nuclear displacements will periodically vanish.

We also note that the each contribution to the time signal in [Equation 7.13](#) will appear at $(E_a, E_b - E_c)$ in the spectrum, and will oscillate at $(E_a - E_b)$ in t_2 . In principle, therefore, it is possible to observe the dephasing that causes both exciton-site decoherence and exciton-polaron formation in the t_2 behaviour of the spectrum: states oscillating at different frequencies in t_2 can overlap at the same E_1 and E_3 in the 2D spectra. In practice, we have seen no decay in the Rabi oscillations as a function of t_2 , however, and so can conclude that we have not observed any manifestation of exciton-site decoherence or exciton-polaron formation using this spectroscopy.

Exciton localisation is visible in 2D ECS spectra, however, and manifests itself in the broadening of peaks corresponding to states from which population is being lost. Unfortunately, the incoherent nature of this relaxation means that the LEGS onto which the

system relaxes can not be identified. We can understand this by considering a two level system, and the effect of averaging over many quantum jumps:

1. At $t = 0$ we are solely in the excited state, such that $|\Psi\rangle = |1\rangle$.
2. Evolving this for a time Δt gives $|\Psi(t = \Delta t)\rangle = e^{-iE_1\Delta t} |1\rangle$.
3. De-exciting a small amount of amplitude means that the phase of the excited state is imparted onto the ground: $|\Psi(t = \Delta t)\rangle = (1 - c_1)e^{-iE_1\Delta t} |1\rangle + c_1e^{-iE_1\Delta t} |0\rangle$, where c_1 is real.
4. Evolving for a further time Δt gives:

$$|\Psi(t = 2\Delta t)\rangle = (1 - c_1)e^{-i2E_1\Delta t} |1\rangle + c_1e^{-iE_1\Delta t - iE_0\Delta t} |0\rangle$$

5. De-exciting a further small amount of amplitude gives:

$$|\Psi(t = 2\Delta t)\rangle = (1 - c_1 - c_2)e^{-i2E_1\Delta t} |1\rangle + (c_1e^{-iE_1\Delta t - iE_0\Delta t} + c_2e^{-i2E_1\Delta t}) |0\rangle$$

Continuing in this manner gives

$$|\Psi(t = n\Delta t)\rangle = \left(1 - \sum_{j=1}^n c_j\right) e^{-inE_1\Delta t} |1\rangle + \sum_{j=1}^n c_j e^{-(jE_1 + (n-j)E_0)\Delta t} |0\rangle \quad (7.14)$$

All contributions rotate at E_0 once in the ground state, but the fact that $E_1 \neq E_0$ means that the phases of all these contributions are uniformly distributed in the range $[0, 2\pi]$. The slow nature of the decay, such that $c_n \approx c_{n+1}$, means that these terms give near perfect complete destructive interference. While a simplification of the large system we consider, this is a useful tool in understanding why we can not see any contributions from the LEGS in the final spectrum, yet alone identify which of the LEGS is preferentially relaxed onto.

Chapter 8: Conclusions

The aim of this research was to understand how the ultrafast dynamics of single chain polymers present themselves in two dimensional spectroscopy.

We find that there is no direct evidence of exciton-site decoherence or exciton-polaron formation in a 2D ECS spectrum. The driving force behind these two phenomena (rapid destructive interference of eigenfunction coefficients) can in principle be detected in the waiting time (t_2) behaviour of the spectrum. We have observed no damping in the Rabi oscillations of peaks however, and thus have not detected the manifestation of either of these processes.

Vibrational relaxation and exciton localisation present themselves in the spectrum as lifetime broadening. The incoherent nature of the localisation means, however, that the chromophores onto which the system localises can not be detected.

Inhomogeneous broadening, and lifetime-broadening in t_1 and t_3 , have both been observed in this work, leading to diagonal, vertical and horizontal peak broadening respectively. In future work, the effects of homogenous broadening may be investigated: the Hamiltonian is not truly stationary over the timescale of the dynamics, and so fluctuations in the onsite energies and nearest neighbour couplings will lead to homogenous, or anti-diagonal, broadening, and a lineshape that changes as a function of t_2 .⁴³

Further dynamical processes that should be studied using the simulation of 2D ECS developed in this work include interchain transfer between coupled chains and the effects of coupling between the exciton and torsional modes.

Finally, inclusion of more realistic pulse shapes would allow a better approximation of experimentally obtained spectra.

Bibliography

- (1) Downs, A. J.; Gardner, C. J. *J. Chem. Soc., Dalt. Trans.* **1984**, 2127.
- (2) Burroughes, J. H.; Bradley, D. D. C.; Brown, A. R.; Marks, R. N.; Mackay, K.; Friend, R. H.; Burns, P. L.; Holmes, A. B. *Nature* **1990**, *347*, 539.
- (3) Skotheim, T. A.; Elsenbaumer, R. L.; Reynolds, J. R., *Handbook of Conducting Polymers*, 2nd ed.; Marcel Dekker, Inc.: Boca Raton, 1998.
- (4) Barford, W., *Electronic and Optical Properties of Conjugated Polymers*, 2nd; Oxford University Press: Oxford, 2013.
- (5) Peng, H.; Sun, X.; Weng, W.; Fang, X., *Polymer Materials for Energy and Electronic Applications*; Academic Press: Cambridge, 2017.
- (6) Li, J.; Sun, N.; Guo, Z.-X.; Li, C.; Li, Y.; Dai, L.; Zhu, D.; Sun, D.; Cao, Y.; Fan, L. *J. Phys. Chem. B* **2002**, *106*, 11509.
- (7) Chen, P.; Ma, Y.; Zheng, Z.; Wu, C.; Wang, Y.; Liang, G. *Nat. Commun.* **2019**, *10*, 1192.
- (8) Abe, S.; Schreiber, M.; Su, W. P.; Yu, J. *Phys. Rev. B* **1992**, *45*, 9432.
- (9) Mannouch, J. R.; Barford, W.; Al-Assam, S. *J. Chem. Phys.* **2018**, *148*, 034901.
- (10) Condon, E. U. *Phys. Rev.* **1928**, *32*, 858.
- (11) Sariciftci, N. S., *Primary Photoexcitations in Conjugated Polymers: Molecular Exciton Versus Semiconductor Band Model*; World Scientific: Linz, 1998.
- (12) Wannier, G. H. *Phys. Rev.* **1937**, *52*, 191.

- (13) Barford, W.; Paiboonvorachat, N. *J. Chem. Phys.* **2008**, *129*, 164716.
- (14) Frenkel, J. *Phys. Rev.* **1931**, *37*, 17.
- (15) Dirac, P. A. M. *Proc. R. Soc. A Math. Phys. Eng. Sci.* **1927**, *114*, 243.
- (16) Surján, P. R., *Second Quantized Approach to Quantum Chemistry : an Elementary Introduction*; Springer Berlin Heidelberg: Berlin, 1989.
- (17) Atkins, P. W.; De Paula, J., *Atkins' Physical Chemistry*, 9th ed.; Oxford University Press: Oxford, 2010.
- (18) Tozer, O. R.; Barford, W. *J. Phys. Chem. A* **2012**, *116*, 10310.
- (19) Anderson, P. W. *Phys. Rev.* **1958**, *109*, 1492.
- (20) Makhov, D. V.; Barford, W. *Phys. Rev. B* **2010**, *81*, 165201.
- (21) Malyshev, A. V.; Malyshev, V. A. *Phys. Rev. B* **2001**, *63*, 195111.
- (22) Sterpone, F.; Rossky, P. J. *J. Phys. Chem. A* **2008**, *112*, 4983.
- (23) Tretiak, S.; Saxena, A.; Martin, R. L.; Bishop, A. R. *Phys. Rev. Lett.* **2002**, *89*, 097402.
- (24) Bittner, E. R.; Rossky, P. J. *J. Chem. Phys.* **1995**, *103*, 8130.
- (25) Hwang, H.; Rossky, P. J. *J. Chem. Phys. B* **2004**, *108*, 6723.
- (26) Holstein, T.; T. *Ann. Phys. (N. Y.)* **1959**, *8*, 343.
- (27) Friedman, L.; Holstein, T. *Ann. Phys. (N. Y.)* **1963**, *21*, 494.
- (28) Barford, W.; Marcus, M. *J. Chem. Phys.* **2014**, *141*, 164101.
- (29) Weiss, U., *Quantum Dissipative Systems*. 4th ed.; World Scientific: Singapore, 2012.
- (30) Lindblad, G. *Commun. Math. Phys.* **1976**, *48*, 119.
- (31) Pearle, P. *Eur. J. Phys.* **2012**, *33*, 805.
- (32) Daley, A. J. *Adv. Phys.* **2014**, *63*, 77.
- (33) Barchielli, A.; Vacchini, B. *New J. Phys.* **2015**, *17*, 083004.

- (34) Grage, M. M.-L.; Zaushitsyn, Y.; Yartsev, A.; Chachisvilis, M.; Sundström, V.; Pullerits, T. *Phys. Rev. B* **2003**, *67*, 205207.
- (35) Hwang, I.; Scholes, G. D. *Chem. Mater.* **2011**, *23*, 610.
- (36) Barford, W.; Bittner, E. R.; Ward, A. *J. Phys. Chem. A* **2012**, *116*, 10319.
- (37) Heller, E. J. *J. Chem. Phys.* **1978**, *68*, 2066.
- (38) Heller, E. J. *J. Chem. Phys.* **1978**, *68*, 3891.
- (39) Tekavec, P. F.; Lott, G. A.; Marcus, A. H. *J. Chem. Phys.* **2007**, *127*, 214307.
- (40) Ovchinnikov, M.; Apkarian, V. A.; Voth, G. A. *J. Chem. Phys.* **2001**, *114*, 7130.
- (41) Kleckner, I. R.; Foster, M. P. *Biochim. Biophys. Acta* **2011**, *1814*, 942.
- (42) Cho, M., *Two-Dimensional Optical Spectroscopy*; CRC Press: New York, 2009.
- (43) Hamm, P.; Zanni, M. T., *Concepts and methods of 2d infrared spectroscopy*; Cambridge University Press: Cambridge, 2011.
- (44) Khalil, M.; Demirdöven, N.; Tokmakoff, A. *J. Phys. Chem. A* **2003**, *107*, 5258.
- (45) Tannor, D. J., *Introduction to Quantum Mechanics: a Time-Dependent Perspective*; University Science Books: Harvard, 2007.
- (46) Al-Assam, S.; Clark, S. R.; Jaksch, D. **2016**, DOI: [10.1088/1742-5468/aa7df3](https://doi.org/10.1088/1742-5468/aa7df3).
- (47) Daley, A. J.; Kollath, C.; Schollwöck, U.; Vidal, G. *J. Stat. Mech. Theory Exp.* **2004**, *2004*, 04005.
- (48) Vidal, G. *Phys. Rev. Lett.* **2003**, *91*, 147902.
- (49) Vidal, G. *Phys. Rev. Lett.* **2004**, *93*, 040502.
- (50) Schollwöck, U. *The Density-Matrix Renormalization Group in the Age of Matrix Product States*; tech. rep.; 2011.
- (51) White, S. R.; Feiguin, A. E. *Phys. Rev. Lett.* **2004**, *93*, 076401.

- (52) Sabin, W. E., *Discrete-Signal Analysis and Design*; Wiley-Interscience: Hoboken, 2008.
- (53) Smith, J. O., *Mathematics of the Discrete Fourier Transform (DFT): with Audio Applications*, 2nd ed.; W3K Publishing: 2007.
- (54) Briggs, W. L.; Henson, V. E., *The DFT: An Owner's Manual for the Discrete Fourier Transform*; Society for Industrial and Applied Mathematics: Philadelphia, 1995.
- (55) Lang, I. G.; Firsov, Y. A. *J. Exptl. Theor. Phys.* **1963**, 16, 1843.
- (56) Rabi, I. I.; Millman, S.; Kusch, P.; Zacharias, J. R. *Phys. Rev.* **1939**, 55, 526.